CHALMERS
UNIVERSITY OF TECHNOLOGY

Spatial Multiplexing Over LOS Channels With Circular Arrays: Analysis and Design

Citation for the original published paper (version of record):
Ding, L., Devassy, R., Vilenskiy, A. et al (2026). Spatial Multiplexing Over LOS Channels With Circular Arrays: Analysis and Design. IEEE Transactions on Wireless Communications, 25: 4936-4952. http://dx.doi.org/10.1109/TWC.2025.3615506

(article starts on next page)

Spatial Multiplexing Over LOS Channels With Circular Arrays: Analysis and Design

Liqin Ding, Rahul Devassy, Artem R. Vilenskiy, *Senior Member, IEEE*, Mikael Coldrey, Thomas Eriksson, *Member, IEEE*, and Erik G. Ström, *Fellow, IEEE*

***Abstract*—This paper models the line-of-sight (LOS) channel between two continuous circular antennas (CCAs) as a bounded linear normal operator whose kernel is defined by a deployment parameter: the product of the antenna radii divided by the product of the wavelength and transmission distance. Eigen-decomposition reveals that orbital angular momentum (OAM) serves as the eigenmodes, with eigenvalues given by Bessel functions of the first kind, evaluated at the deployment parameter. By linking discrete circular arrays to CCAs through spatial sampling, we derive analytical expressions for the singular values of the LOS multiple-input multiple-output (MIMO) channel. The analysis considers two configurations: one where receive antennas form a single uniform circular array (UCA) with a rotational angular offset, and one with multiple sub-UCAs having different angular offsets, in both cases with the number of receive antennas being an integer multiple of the transmit antennas. For each setup, discrete Fourier transform (DFT)-based transceiver structures are proposed to achieve channel capacity. Numerical evaluations reveal: (i) The number of effective spatial degrees of freedom generally increases with the deployment parameter, but not monotonically (for fixed angular offsets); (ii) Channel capacity does not necessarily increase with the deployment parameter when the number of antennas is fixed; (iii) Angular offset significantly impacts performance when the number of antennas is small relative to the parameter; (iv) With a large number of antennas, the singular values of both configurations approach the CCA singular values, and the impact of angular offsets diminishes; (v) The non-uniform configuration studied in this paper yield small or no gains compared to the uniform configuration when angular offsets are optimized.**

***Index Terms*—LOS MIMO, UCA, OAM, eigenmodes, SVD.**

Received 30 May 2024; revised 3 January 2025 and 7 August 2025; accepted 19 September 2025. Date of publication 6 October 2025; date of current version 22 December 2025. This work was supported by the Framework of the EUREKA EURIPIDES2 InnoStar Project under Grant Diarienummer 2021-0405. An earlier version of this paper was presented in part at the IEEE 33rd Annual International Symposium on PIMRC [DOI: 10.1109/PIMRC54779.2022.9977586]. The associate editor coordinating the review of this article and approving it for publication was L. Simic. *(Corresponding author: Liqin Ding.)*

Liqin Ding was with the Department of Electrical Engineering, Chalmers University of Technology, 412 96 Gothenburg, Sweden. She is now with Ericsson Research, Ericsson AB, 223 62 Lund, Sweden (e-mail: liqin.ding@ericsson.com).

Rahul Devassy and Mikael Coldrey are with Ericsson Research, Ericsson AB, 417 56 Gothenburg, Sweden.

Artem R. Vilenskiy was with the Department of Electrical Engineering, Chalmers University of Technology, 412 96 Gothenburg, Sweden. He is now with XPANCEO Research on Natural Science, Dubai, United Arab Emirates.

Thomas Eriksson and Erik G. Ström are with the Department of Electrical Engineering, Chalmers University of Technology, 412 96 Gothenburg, Sweden.

Digital Object Identifier 10.1109/TWC.2025.3615506

I. Introduction

THE demand for ever-higher data rates is driving wireless communications into the millimeter-wave (mmWave) and terahertz spectrum, where non-line-of-sight (NLOS) communication becomes increasingly challenging. Interestingly, spatial multiplexing, a key method to boost spectral efficiency and data rates, can also thrive in line-of-sight (LOS) conditions when antennas or arrays are large enough. From a spatial perspective, a large transmit antenna or array excites a nonzero spatial bandwidth in the signal received, unlocking spatial degree-of-freedom (DOF) in the LOS channel [2], [3]. This has brought LOS multiple-input multiple-output (MIMO) communication [4], [5], [6] back into the spotlight.

LOS MIMO systems with uniform circular arrays (UCAs) have garnered significant attention in recent literature, as exemplified by studies such as [7], [8], [9], and [10] and others cited therein. This interest is largely due to the capability of UCAs to exploit orbital angular momentum (OAM) modes [11], [12], [13] with relatively simple processing techniques. Several experimental implementations have been reported [14], [15], [16]. The performance of LOS MIMO systems is generally affected by the geometry of the transmit and receive arrays and is sensitive to variations in transmission distance and misalignments such as tilt and rotation [6], [17]. When UCAs are employed, these geometrical sensitivities are more pronounced and distinct compared to uniform linear arrays (ULAs) or uniform rectangular arrays (URAs) [18], [19]. Specifically, as UCAs experience tilt or rotational misalignment, not only do the number of available spatial subchannels change, but the singular values associated with these subchannels are also affected. There has also been some research on the design of transmit/receive schemes under certain misalignment conditions [20], [21], as well as choosing better parameters [22] or non-uniform antenna placement [23] to improve robustness to misalignment. It is important to note that while there is extensive literature on NLOS MIMO with UCAs, this topic is beyond the scope of our paper and will not be addressed here. In our previous conference paper [1], we derived the singular values of the LOS UCA channel under conditions of perfect alignment, assuming an equal number of antenna elements on both the transmitting and receiving sides. This derivation was based on an eigenmode analysis of the LOS channel between two continuous circular antennas (CCAs), confirming the role of OAM modes as the continuous channel eigenmodes. We provided expressions for these eigenvalues using Bessel functions of the first kind. By

relating the UCA channel to the CCA channel through spatial sampling, we identified that the discrete eigenvalues depend on the continuous eigenvalues through aliasing. This perspective not only explains the behavior of the UCA channel but also clarifies the underlying reasons for its specific characteristics.

In this paper, we extend our study to more general scenarios where the number of antennas in the transmitting and the receiving UCAs may differ, the receiving array may have an angular offset, and the receiving antenna elements may be arranged as multiple sub-UCAs rather than a single large UCA. We provide a tutorial-style of the singular values of the generalized UCA channel, utilizing an analytical method different from that in [1]. Our specific technical contributions include:

- We establish a bounded linear normal operator representing the CCA channel. An eigendecomposition of this operator is derived, providing a precise characterization of the DOFs and yielding analytical expressions for the singular value decomposition (SVD).
- We decompose the channel matrix for a general $N_t \times N_r$ UCA system into an infinite sum of weighted rank-1 matrices, highlighting the multidiagonal nature of the coupling coefficient matrix generated by discrete Fourier transform (DFT) precoding and combining. We provide analytical expressions for the matrix elements.
- We derive analytical expressions for the singular values of the $N_t \times LN_t$ LOS channel when the transmitter is a UCA, and the receiver is either a UCA or comprises L sub-UCAs offset in angle and located on the same circle. Additionally, we propose two DFT-based, capacity-achieving transceiver structures for these configurations.

The derived expressions for singular values lead directly to expressions for the Shannon channel capacity, as detailed in the paper, and can be used to validate claims in the existing literature. They also offer guidance for the practical implementation of such systems, as demonstrated and examined in our numerical study. These results address questions about choosing geometrical parameters and designing array layouts for more robust systems. Notably, the derived expressions are verified using full-wave electromagnetic (EM) simulations with realistic dipole antennas in our numerical analysis.

Notation: $(\cdot)^{\mathrm{T}}$ denotes the transpose, and $(\cdot)^{\mathrm{H}}$ denotes the conjugate transpose. $\mathbb{Z}$, $\mathbb{Z}^+ = \{1, 2, \ldots\}$, and $\mathbb{N} = \{0, 1, \ldots\}$ represent the sets of integers, positive integers, and non-negative integers, respectively. The set $A + B\mathbb{Z}$, where A and B are integers, is defined as $\{A + kB : k \in \mathbb{Z}\}$. The greatest common divisor of the integers a and b is denoted by $\gcd(a, b)$, and their least common multiple is denoted by $\mathrm{lcm}(a, b)$.

The paper is organized into six sections and three appendices. In Section II, we define and analyze the CCA channel, focusing on its DOFs and capacity. A similar analysis for the UCA channel is presented in Section III. Section IV introduces and examines two optimal receiving structures. Numerical results are provided in Section V, and the paper concludes with Section VI. Proofs of Theorems 2 and 3, as well as a statement regarding when the UCA channel may lose one DOF, are provided in Appendices VI–VI.

II. The CCA Channel

We begin by examining the wireless channel between two CCAs under free-space propagation conditions, which we refer to as the *CCA channel*. Key findings on this channel were previously presented [1]. In this paper, we adopt a functional analysis-based approach, differing from [1], to derive the eigendecomposition of the linear operator representing the CCA channel. The outcome leads to an estimate of the effective number of DOFs and an unsorted SVD. Finally, we provide a capacity analysis of the CCA channel.

A. CCA Channel Formulation

The geometric arrangement of the two perfectly aligned CCAs is illustrated in Fig. 1. We denote the source antenna as $\mathcal{A}_t$ and the receiving antenna as $\mathcal{A}_r$, with radii R_t and R_r, respectively. We locate the origin of the coordinate system at the center of $\mathcal{A}_t$ and let the x-y-plane contain $\mathcal{A}_t$. The z-axis passes through the center of $\mathcal{A}_r$ at $(0, 0, D)^{\mathrm{T}}$. Both antennas are assumed to consist of Hertzian dipoles, allowing for continuous electrical current. We focus on time-harmonic current sources using the $\exp(j\omega t)$ convention, with the assumptions that (i) $D \gg \lambda$, where λ is the wavelength corresponding to the angular frequency ω, and (ii) $D \gg \max(R_t, R_r)$. Under these assumption, we derive an analytical description of the CCA channel.

We denote the current density at a point $\mathbf{s} \in \mathcal{A}_t$ as $\mathcal{J}(\mathbf{s}) \in \mathbb{C}^{3\times 1}$. The electric field at a point $\mathbf{p} \in \mathcal{A}_r$ can be expressed as

$$\mathcal{E}(\mathbf{p}) = \int_{\mathcal{A}_t} \mathcal{G}(\mathbf{p} - \mathbf{s})\mathcal{J}(\mathbf{s})\, \mathrm{d}\mathbf{s}, \tag{1}$$

where $\mathcal{G} : \mathbb{R}^{3\times 1} \to \mathbb{C}^{3\times 3}$ is the dyadic Green's function, given as follows [24, Appendix I] [2]

$$\mathcal{G}(\mathbf{r}) = \frac{-j\omega\mu}{4\pi} \exp(-jk_0 r) \cdot \left[\underbrace{\frac{1}{r}\left(\mathbf{I}_3 - \hat{\mathbf{r}}\hat{\mathbf{r}}^{\mathrm{T}}\right)}_{\text{"radiative"}} + \underbrace{\left(\frac{j}{k_0 r^2} - \frac{1}{k_0^2 r^3}\right)\left(\mathbf{I}_3 - 3\hat{\mathbf{r}}\hat{\mathbf{r}}^{\mathrm{T}}\right)}_{\text{"non-radiative"}} \right],$$

where $j = \sqrt{-1}$, μ is the permeability of free space, $\mathbf{r} = \mathbf{p} - \mathbf{s}$, $r \triangleq \|\mathbf{r}\|$, $\hat{\mathbf{r}} = (\hat{r}_{\mathrm{x}}, \hat{r}_{\mathrm{y}}, \hat{r}_{\mathrm{z}})^{\mathrm{T}} \triangleq \mathbf{r}/r$, and $\mathbf{I}_3$ is a 3×3 identity matrix. The non-radiative term in $\mathcal{G}$ decays rapidly with r. Under the assumption $D \gg \lambda$, it becomes negligible compared to the radiative term, leading to the approximation

$$\mathcal{G}_{\mathrm{F}}(\mathbf{r}) = \frac{-j\omega\mu}{4\pi r} e^{-j\frac{2\pi}{\lambda}r} \left(\mathbf{I}_3 - \hat{\mathbf{r}}\hat{\mathbf{r}}^{\mathrm{T}}\right). \tag{2}$$

For simplicity, we assume that the Hertzian dipoles consisting $\mathcal{A}_t$ and $\mathcal{A}_r$ are oriented along the x-axis direction, allowing $\mathcal{J}(\mathbf{s})$ to be expressed as $\mathcal{J}_{\mathrm{x}}(\mathbf{s})\hat{\mathbf{e}}_{\mathrm{x}}$, where $\hat{\mathbf{e}}_{\mathrm{x}} = (1, 0, 0)^{\mathrm{T}}$. $\mathcal{A}_r$ only perceives $\mathcal{E}_{\mathrm{x}}(\mathbf{p})$, the electric field component in the $\hat{\mathbf{e}}_{\mathrm{x}}$ direction[1].

[1]The electric field components in the y and z directions can be expressed similarly, but with $(1 - \hat{r}_{\mathrm{x}}^2)$ in $\mathcal{G}_{\mathrm{x,x}}$ replaced by $(0 - \hat{r}_{\mathrm{x}}\hat{r}_{\mathrm{y}})$ and $(0 - \hat{r}_{\mathrm{x}}\hat{r}_{\mathrm{z}})$, respectively. As $D \to \infty$ for fixed R_t and R_r, $\hat{r}_{\mathrm{x}} \to 0$ and $\hat{r}_{\mathrm{y}} \to 0$, making the y and z components negligible.

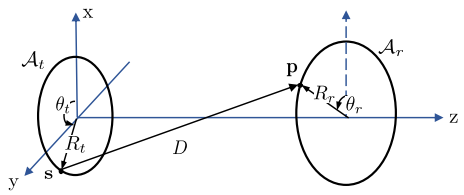

Fig. 1. LOS channel between two perfectly aligned circular arrays.

As shown in Fig. 1, we use two angles, θ_t and θ_r, both in the range $[0, 2\pi)$, to parameterize $\mathbf{s}$ and $\mathbf{p}$. Accordingly, we have $\mathbf{s}(\theta_t) = (R_t \cos\theta_t, R_t \sin\theta_t, 0)^{\mathrm{T}}$, $\mathbf{p}(\theta_r) = (R_r \cos\theta_r, R_r \sin\theta_r, D)^{\mathrm{T}}$,

$$r(\theta_r, \theta_t) = D\sqrt{1 + \frac{R_t^2 + R_r^2 - 2R_tR_r\cos(\theta_r - \theta_t)}{D^2}}, \tag{3}$$

$$\begin{bmatrix} \hat{r}_{\mathrm{x}}(\theta_r, \theta_t) \\ \hat{r}_{\mathrm{y}}(\theta_r, \theta_t) \\ \hat{r}_{\mathrm{z}}(\theta_r, \theta_t) \end{bmatrix} = \frac{1}{r(\theta_r, \theta_t)} \begin{bmatrix} R_r\cos\theta_r - R_t\cos\theta_t \\ R_r\sin\theta_r - R_t\sin\theta_t \\ D \end{bmatrix}, \tag{4}$$

$\mathbf{s}'(\theta_t) = \frac{\mathrm{d}}{\mathrm{d}\theta_t}\mathbf{s}(\theta_t) = (-R_t\sin\theta_t, R_t\cos\theta_t, 0)^{\mathrm{T}}$, and $\mathrm{d}\mathbf{s} = \|\mathbf{s}'(\theta_t)\|\,\mathrm{d}\theta_t = R_t\,\mathrm{d}\theta_t$. We treat $\mathcal{J}_{\mathrm{x}}(\cdot)$ and $\mathcal{E}_{\mathrm{x}}(\cdot)$ as functions mapping $[0, 2\pi)$ to $\mathbb{C}$. Using (1) and (2), we derive the relationship

$$\mathcal{E}_{\mathrm{x}}(\theta_r) = \int_0^{2\pi} R_t\,\mathcal{G}_{\mathrm{x,x}}(\theta_r, \theta_t)\mathcal{J}_{\mathrm{x}}(\theta_t)\,\mathrm{d}\theta_t, \tag{5}$$

where

$$\mathcal{G}_{\mathrm{x,x}}(\theta_r, \theta_t) = \frac{-j\omega\mu}{4\pi r(\theta_r, \theta_t)}[1 - \hat{r}_{\mathrm{x}}^2(\theta_r, \theta_t)]e^{-j\frac{2\pi}{\lambda}r(\theta_r, \theta_t)}. \tag{6}$$

We observe that $r(\theta_r, \theta_t)$ influences both the amplitude and phase of $\mathcal{G}_{\mathrm{x,x}}(\theta_r, \theta_t)$. Under the assumption $D \gg \max(R_t, R_r)$, we can apply the first-order Taylor approximation $\sqrt{1+x} \approx 1 + \frac{x}{2}$ for small x to (3), yielding

$$r(\theta_r, \theta_t) \approx D + \frac{R_t^2 + R_r^2}{2D} - \frac{R_tR_r}{D}\cos(\theta_r - \theta_t). \tag{7}$$

From (6) and (7), it is evident that $\mathcal{G}_{\mathrm{x,x}}(\theta_r, \theta_t)$ remains approximately constant if D is so large that $R_tR_r/D \ll \lambda$. In this scenario, the electric field $\mathcal{E}_{\mathrm{x}}(\theta_r)$ does not vary with θ_r. However, when D is not excessively large, such that R_tR_r/D is at least comparable to λ (the criterion will become clearer later), the phase change in $e^{-j\frac{2\pi}{\lambda}r(\theta_r, \theta_t)}$ within $\mathcal{G}_{\mathrm{x,x}}(\theta_r, \theta_t)$ becomes significant enough to introduce substantial variation in $\mathcal{E}_{\mathrm{x}}(\theta_r)$. This result in additional spatial DOFs to be explored. Conversely, the amplitude variation of $\mathcal{G}_{\mathrm{x,x}}(\theta_r, \theta_t)$ is limited and has relatively minimal impact on DOF. Therefore, we use the approximations $r(\theta_r, \theta_t) \approx D$ and $\hat{r}_{\mathrm{x}} \approx 0$ (as $\hat{\mathbf{r}} \approx \hat{\mathbf{e}}_{\mathrm{z}}$) for the amplitude part, while applying (7) solely to the complex exponential term. Combined, these approximations yield

$$\mathcal{G}_{\mathrm{x,x}}(\theta_r, \theta_t) \approx \alpha\, e^{j2\pi\frac{R_tR_r}{\lambda D}\cos(\theta_r - \theta_t)} \tag{8}$$

where α is a constant given by

$$\alpha \triangleq \frac{-j\omega\mu}{4\pi D}e^{-j\frac{2\pi}{\lambda}[D + (R_t^2 + R_r^2)/2D]}. \tag{9}$$

B. Linear Operator Analysis

Consider the space of square-integrable complex functions over the interval $[0, 2\pi)$, denoted by $\mathcal{L}^2([0, 2\pi))$. The inner product in this space is defined as

$$\langle u, v\rangle \triangleq \int_0^{2\pi} u(\theta)v^*(\theta)\,\mathrm{d}\theta, \tag{10}$$

where $v^*(\theta)$ is the complex conjugate of $v(\theta)$. Accordingly, the norm of a function $u(\cdot) \in \mathcal{L}^2([0, 2\pi))$ is defined as $\|u\| \triangleq \sqrt{\langle u, u\rangle}$. We will consider the linear operator A with domain $\mathcal{L}^2([0, 2\pi))$ and the mapping

$$(\mathsf{A}x)(\phi) = \int_0^{2\pi} h(\phi - \theta)x(\theta)\,\mathrm{d}\theta, \tag{11}$$

where the kernel

$$h(\cdot) \triangleq e^{j\beta\cos(\cdot)} \tag{12}$$

is parameterized by a positive real number β. Note that A is a bounded operator, as the kernel h is continuous and bounded. If we let $x(\cdot) = \mathcal{J}_x(\cdot)$ and

$$\beta = 2\pi\frac{R_tR_r}{\lambda D}, \tag{13}$$

then $R_t\alpha \cdot (\mathsf{A}x)(\theta_r)$ equals the electric field described in (5) assuming $\mathcal{G}_{\mathrm{x,x}}(\theta_r, \theta_t)$ is given by (8). We refer to A as an *energy-normalized* linear operator representing the CCA channel.

As seen from (13), β depends on the geometry and wavelength. Hence, we can view β as fixed for a given deployment or as a parameter that can be optimized, e.g., by adjusting the transmit and receive antenna radii (the hop distance and wavelength are often fixed in practice). Of course, physical constraints will limit the feasible values of β.

1) Eigendecomposition: The linear operator A is both bounded and normal[2]. Therefore, A allows for eigendecompositions of the form

$$\mathsf{A}x = \sum_{n\in\mathbb{Z}} \lambda_n\psi_n\langle x, \psi_n\rangle. \tag{14}$$

where $\{\psi_n\}$ is the set of eigenfunctions and λ_n is the complex eigenvalue associated with ψ_n. Note that the operator $z\mathsf{A}$, for $z \in \mathbb{C}$, has the same eigenfunctions as A but with scaled eigenvalues $z\lambda_n$. Explicit expressions of the eigenfunctions and eigenvalues for A are provided in the following proposition.

[2]The operator A is bounded if there exists a constant $c < \infty$ such that $\|\mathsf{A}x\| < c\|x\|$ for all $x \in \mathcal{L}^2([0, 2\pi))$ [25, Sec. 6.1]. Moreover, A is normal if it commutes with its Hermitian adjoint $\mathsf{A}^\dagger$. Specifically, for any $x, y \in \mathcal{L}^2([0, 2\pi))$, the Hermitian adjoint operator $\mathsf{A}^\dagger$ is uniquely defined by the relation $\langle y, \mathsf{A}x\rangle = \langle \mathsf{A}^\dagger y, x\rangle$ [25, Eq. (113)]. The Hermitian adjoint of A is given by the mapping

$$(\mathsf{A}^\dagger y)(\theta) = \int_0^{2\pi} e^{-j\beta\cos(\theta - \phi)}y(\phi)\,\mathrm{d}\phi.$$

It is straightforward to verify that $\mathsf{A}^\dagger\mathsf{A} = \mathsf{A}\mathsf{A}^\dagger$ (A commutes with $\mathsf{A}^\dagger$). The spectral theorem for normal operators follows from the spectral theorem for self-adjoint operators, as both $\mathsf{A}^\dagger\mathsf{A}$ and $\mathsf{A}\mathsf{A}^\dagger$ are self-adjoint operators and share the same eigendecomposition with real eigenvalues. Direct proofs of the spectral theorem for normal operators are available in [26] and [27].

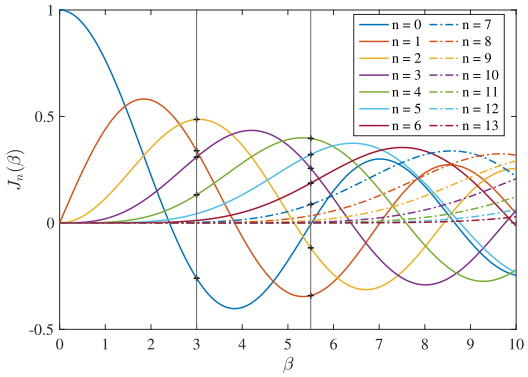

Fig. 2. The value of $J_n(\beta)$ for non-negative orders from 0 to 13. For $\beta = 3$ and $\beta = 5.5$, the orders that yield $|J_n(\beta)| \geq 0.1 \max_n |J_n(\beta)|$ are marked using +.

Proposition 1: With the inner product defined in (10), the linear operator $A : \mathcal{L}^2\big([0, 2\pi)\big) \to \mathcal{L}^2\big([0, 2\pi)\big)$ specified by the mapping in (11) has orthonormal eigenfunctions given by

$$\psi_n(\theta) \triangleq (2\pi)^{-\frac{1}{2}} e^{jn\theta}, \quad n \in \mathbb{Z}, \tag{15}$$

and eigenvalues given by

$$\lambda_n(\beta) = 2\pi j^n J_n(\beta), \quad n \in \mathbb{Z}, \tag{16}$$

where $J_n(\cdot)$ represents the Bessel function of the first kind of order n, defined as

$$J_n(\beta) \triangleq \frac{1}{2\pi} \int_{-\pi}^{\pi} e^{j(\beta \sin\theta - n\theta)} \, \mathrm{d}\theta. \tag{17}$$

Proof: The proof is based on the following key points:

1) The infinite set $\{\psi_n\}_{n\in\mathbb{Z}}$ forms a complete orthonormal system of $\mathcal{L}^2\big([0, 2\pi)\big)$ [28, Definition 8.2.1]. Orthonormality means that $\|\psi_n\| = 1$ and $\langle \psi_n, \psi_m \rangle = 0$ for any $n \neq m$.
2) Due to its periodic nature with a period of 2π, $h(\theta)$ can be expressed by Fourier series expansion [1]:

$$h(\theta) = \sum_{n\in\mathbb{Z}} j^n J_n(\beta) e^{jn\theta}, \tag{18}$$

where $J_n(\cdot)$ is the Bessel function of the first kind of order n.

The orthogonality of $\{e^{jn\theta}\}$ ensures that $\{\psi_n(\theta)\}$ is the set of orthonormal eigenfunctions of A, and the eigenvalues are given by (16).□

2) Effective DOF: Proposition 1 shows that the harmonics of θ with a fundamental frequency of $1/2\pi$, also known as OAM modes, form the eigenmodes of the CCA channel[3]. The eigenvalues are determined by integer-order Bessel functions of the first kind evaluated at $\beta = 2\pi R_t R_r / \lambda D$. For any integer n, the relation $J_{-n}(\beta) = (-1)^n J_n(\beta)$ holds. As $|n|$ increases, the amplitude of $J_n(\beta)$ decreases rapidly and approaches zero[4]. Additionally, according to *Neumann's addition theorem* [29, Eq. 9.1.76], we have

$$\sum_{n\in\mathbb{Z}} J_n^2(\beta) = 1 \tag{19}$$

for any β. These properties of Bessel functions imply that, although the eigendecomposition of A theoretically includes an infinite number of terms, only a finite subset is associated with significant eigenvalues.

When $\beta \to 0$, $J_0(\beta) \approx 1$, and $J_n(\beta) \approx 0$ for all $n \neq 0$, indicating that there is effectively only one DOF in the channel. For large β, the number of effective DOFs can be estimated using Carson's rule: Consider $h(\theta) = e^{j\beta\cos(\theta)}$ as a phase-modulated signal with sinusoidal modulation of frequency $f_m = \frac{1}{2\pi}$, where β is the phase modulation index. Carson's rule gives us a rule-of-thumb estimation of the effective bandwidth of $h(\theta)$ [30, Eq. (5-61)]:

$$W = 2(\beta + 1) f_m, \tag{20}$$

which contains 98% the total signal power. Sampling $h(\theta)$ at intervals of $1/W$ over the range $[0, 2\pi)$ yields approximately $2\pi W = 2(\beta + 1)$ samples[5]. Thus, for large β, the number of effective DOFs is approximately

$$K_{\text{eff}} \approx 2(\beta + 1). \tag{21}$$

In Fig. 2, the plots for $J_n(\beta)$, $n = 0, 1, \ldots, 13$ are shown over the range $\beta \in [0, 10]$. For $\beta = 3$ and $\beta = 5.5$, the orders n such that

$$J_n(\beta)| \geq 0.1 \max_{k\in\{0,\ldots,13\}} |J_k(\beta)|$$

are indicated by + markers. Using this criterion to determine effective DOF (by counting the + markers and considering the corresponding negative orders) results in 9 effective DOFs for $\beta = 3$ and 14 effective DOFs for $\beta = 5.5$. In comparison, (21) estimates approximately 8 and 13 effective DOFs for these β values, respectively.

3) SVD: Proposition 1 directly leads to the unsorted SVD of the operator A, as detailed in the following theorem.

Theorem 1: Consider the linear operator A on $\mathcal{L}^2\big([0, 2\pi)\big)$ defined by the mapping (11). An unsorted SVD of A is given by

$$(\mathsf{A}x)(\theta_r) = \sum_{n\in\mathbb{Z}} \gamma_n(\beta) u_n(\theta_r) \langle x, v_n \rangle, \tag{22}$$

where the left singular functions $u_n(\cdot)$, right singular functions $v_n(\cdot)$, and singular values $\gamma_n(\beta)$ are defined for $n \in \mathbb{Z}$ as

$$u_n(\theta_r) \triangleq (2\pi)^{-\frac{1}{2}} e^{j \arg(\lambda_n(\beta))} e^{jn\theta_r}, \tag{23}$$

$$v_n(\theta_t) \triangleq (2\pi)^{-\frac{1}{2}} e^{jn\theta_t}, \tag{24}$$

$$\gamma_n(\beta) \triangleq |\lambda_n(\beta)| = 2\pi |J_n(\beta)|. \tag{25}$$

Proof: This result follows directly from Proposition 1 by incorporating the phase of λ_n into the right singular functions[6].□

[3]It is also known from the literature that the radiated electric field of a UCA with a very large number of antennas can be approximately expressed as a superposition of OAM modes, with weights given by the Bessel functions of the first kind [12, Eq. (8)].

[4]With β fixed, an asymptotic expression of $J_n(\beta)$ as $n \to \infty$ is $J_n(\beta) \sim \frac{1}{\sqrt{2\pi n}} \left(\frac{e\beta}{2n}\right)^n$ [29, Eq. 9.3.1].

[5]See [3, Eq. (1)] and the discussion following it.

[6]Alternatively, the phase can be incorporated into the left singular functions, resulting in a different form for the SVD. However, the singular values remain the same.

Remark 1: Since $J_{-n}(\beta) = (-1)^n J_n(\beta)$, the singular values $\gamma_n(\beta)$ appear in pairs for $n \neq 0$, meaning $\gamma_n(\beta) = \gamma_{-n}(\beta)$ for $n \in \mathbb{Z}$. Additionally, from (19), we known that for any β,

$$\sum_{n\in\mathbb{Z}} \gamma_n(\beta)^2 = (2\pi)^2. \tag{26}$$

Thus, β influences the distribution of singular values, determining how the total gain $(2\pi)^2$ is allocated among the squared singular values, although the overall gain remains constant irrespective of β. An alternative derivation of (26) can be obtained by integrating the kernel of A, as shown in [31, Eq. 47],

$$\sum_{n\in\mathbb{Z}} \gamma_n(\beta)^2 = \int_0^{2\pi}\int_0^{2\pi} |e^{-j\beta\cos(\theta-\phi)}|^2 \,\mathrm{d}\theta\,\mathrm{d}\phi = (2\pi)^2. \tag{27}$$

The oscillatory nature of Bessel functions causes the relative magnitudes of the singular values to change with β. For any given β, we can sort the singular values in non-increasing order to achieve a sorted SVD. Define $n(k)$ as a bijective mapping from $\mathbb{N}$ to $\mathbb{Z}$ such that $\gamma_{n(0)}(\beta) \geq \gamma_{n(1)}(\beta) \geq \cdots$. With this, the sorted SVD of A is expressed as

$$(\mathsf{A}x)(\theta_r) = \sum_{k\in\mathbb{N}} \gamma_{n(k)}(\beta) u_{n(k)}(\theta_r)\langle x, v_{n(k)}\rangle. \tag{28}$$

As previously mentioned, $\gamma_{n(k)}(\beta)$ rapidly decreases to zero with increasing k due to the behavior of $J_n(\beta)$ for large n.

C. Channel Capacity Analysis

The discussion thus far has centered on the energy-normalized linear operator A, utilizing the inner product defined in (10) for both input and output signals. To evaluate the capacity of the CCA channel, we reintroduce the constant $R_t\alpha$ to restore the channel mapping

$$y(\theta_r) = R_t\alpha\,(\mathsf{A}x)(\theta_r). \tag{29}$$

The CCA channel, assumed to be known at both ends, has singular values $\gamma_n(\beta)R_t|\alpha|$ retains the same singular functions as A. The singular functions from the SVD provide the foundation for an optimal transceiver design, with data rate maximization achieved through power allocation using the water-filling algorithm, given a total transmit power P_T watt.

A distinction must be made between the dimensionless input/output signals of A and the practical signals interacting with the communication system's antenna ports. To address this, we assume the input signal $x(\cdot)$ of A corresponds to a signal with transmit power $\zeta_t\|x\|^2$ watt into $\mathcal{A}_t$, and the output signal $y(\cdot)$ corresponds to received signal power $\zeta_r\|y\|^2$ watt from $\mathcal{A}_r$. For simplicity, we define $G_\mathrm{P} = R_t^2|\alpha|^2\zeta_r/\zeta_t$ such that one watt of transmit power through a spatial subchannel of singular value γ results in $G_\mathrm{P}\gamma^2$ watt of received signal power. Furthermore, when resolving the data signal transmitted over a subchannel, it is assumed that white complex Gaussian noise with a power spectral density of N_0 watt per hertz is added to the received time-domain signal after spatial combining. The noise affecting each subchannel is independent, and the system is considered narrowband, with a bandwidth B hertz centered around $\omega/2\pi$ (where $B \ll \omega/2\pi$).

With these assumptions, the Shannon capacity of the CCA channel can be expressed as follows [32, Chapter 7.1.1]

$$C_\mathrm{CCA} = B\sum_{k\in\mathbb{N}} \log_2\left(1 + \frac{P_k G_\mathrm{P}\gamma_{n(k)}^2(\beta)}{N_0 B}\right) \quad [\mathrm{bit/s}] \tag{30}$$

where the power allocated to the k spatial subchannel, P_k, is determined by water-filling algorithm:

$$P_k = \max\left(\mu - \frac{N_0 B}{G_\mathrm{P}\gamma_{n(k)}^2(\beta)}, 0\right) \tag{31}$$

with μ chosen to satisfy $\sum_k P_k = P_\mathrm{T}$. This analysis highlights an important practical insight: the number of effective spatial subchannels is influenced not only by the singular values $\gamma_{n(k)}(\beta)$ but also by factors such as available transmit power, antenna gains, and noise level. Consequently, we can define the effective DOF of the CCA channel to be the number of subchannels that receive nonzero transmitting power, as determined by (31), at the *reference signal-to-noise ratio (SNR)* given transmit power P_T, defined as

$$\mathrm{SNR}_0(P_\mathrm{T}) \triangleq \frac{P_\mathrm{T}G_\mathrm{P}}{N_0 B}. \tag{32}$$

Note that $\mathrm{SNR}_0(P_\mathrm{T})$ is the received SNR for a single-input single-output (SISO) channel with a channel gain of 1 and a transmit power of P_T.

III. The UCA Channel

We now examine the discrete MIMO channel between two perfectly aligned UCAs with arbitrary numbers of antenna elements (Hertzian dipoles) and angular offset under LOS conditions. This setup is referred to as the *UCA channel*. We formulate the UCA channel matrix by leveraging the linear operator A that represents the CCA channel and analyze the resulting coupling coefficient matrix from discrete DFT precoding and combining, which is lossless. The channel singular values are then derived specifically for the scenario where the number of receive antennas is a multiple of the number of transmit antennas.

A. UCA Channel Matrix Formulation

Consider an $N_t \times N_r$ MIMO system utilizing two perfectly aligned UCAs composed of Hertzian dipoles oriented along the x-axis. We assume $N_t \geq 2$ and $N_r \geq N_t$. The transmitting UCA, $\mathcal{A}_t$, has antenna elements uniformly distributed on a circle with radius R_t at angles given by

$$\theta_{t,n_t} = \frac{2\pi}{N_t}n_t, \quad 0 \leq n_t \leq N_t - 1. \tag{33}$$

Similarly, the receiving UCA, $\mathcal{A}_r$, has its antenna elements uniformly placed on a circle with radius R_r at angles

$$\theta_{r,n_r} = \frac{2\pi}{N_r}n_r + \Delta\theta, \quad 0 \leq n_r \leq N_r - 1. \tag{34}$$

We refer to $\Delta\theta$ as the *relative angular offset* of $\mathcal{A}_r$, with the assumption that $\Delta\theta \in [0, 2\pi/N_r)$. Below, we formulate the $N_r \times N_t$ UCA channel matrix $\mathbf{H}$. For convenience, we use zero-based indexing for the rows and columns of $\mathbf{H}$, meaning that the first row or column has index of 0.

The current density at the n_tth antenna element of $\mathcal{A}_t$ is denoted by $x[n_t]$. We can represent $\mathcal{A}_t$ as a CCA with a current density given by

$$x(\theta_t) = \sum_{n_t=0}^{N_t-1} x[n_t]\delta(\theta_t - \theta_{t,n_t}), \tag{35}$$

where $\delta(\cdot)$ is the Dirac delta function. Substituting this expression into the linear mapping defined in (11), we have

$$y(\theta_r) = (\mathsf{A}x)(\theta_r) = \sum_{n_t=0}^{N_t-1} x[n_t]h(\theta_r - \theta_{t,n_t}), \tag{36}$$

which represents the electric field over an imaginary CCA of radius R_r. The electric field perceived by the n_rth antenna of $\mathcal{A}_r$ is the spatial sample of $y(\theta_r)$ at θ_{r,n_r}:

$$y[n_r] \triangleq y(\theta_{r,n_r}) = \sum_{n_t=0}^{N-1} x[n_t]h(\theta_{r,n_r} - \theta_{t,n_t}). \tag{37}$$

Based on (37), the channel matrix $\mathbf{H}$ is constructed by placing the values of $h(\theta_{r,n_r} - \theta_{t,n_t})$, as defined in (12), into the matrix. Specifically, for each row $n_r = 0, 1, \ldots, N_r - 1$ and column $n_t = 0, 1, \ldots, N_t - 1$,

$$\mathbf{H}[n_r, n_t] = e^{j\beta\cos\left(2\pi\left(\frac{n_r}{N_r} - \frac{n_t}{N_t}\right) + \Delta\theta\right)}. \tag{38}$$

Defining $\mathbf{x} \triangleq (x[0], \ldots, x[N_t-1])^{\mathrm{T}}$ and $\mathbf{y} \triangleq (y[0], \ldots, y[N_r-1])^{\mathrm{T}}$, the input-output relationship for this discrete MIMO system is described by

$$\mathbf{y} = \mathbf{H}\mathbf{x}. \tag{39}$$

Note that $\mathbf{H}$ is energy-normalized similarly to the linear operator A. Since all entries of $\mathbf{H}$ has unit magnitude, it follows that

$$\|\mathbf{H}\|_{\mathrm{F}}^2 = N_t N_r. \tag{40}$$

Moreover, as detailed in the following theorem, we can decompose $\mathbf{H}$ as an infinite sum of scaled outer products of DFT vectors.

Theorem 2: The $N_r \times N_t$ channel matrix $\mathbf{H}$ between two UCAs can be decomposed as an infinite sum of rank-1 matrices:

$$\mathbf{H} = \sum_{n\in\mathbb{Z}} C_n \boldsymbol{\psi}_{N_r,n}\boldsymbol{\psi}_{N_t,n}^{\mathrm{H}}, \tag{41}$$

where

$$C_n = \sqrt{N_t N_r} J_n(\beta) e^{jn\left(\frac{\pi}{2} + \Delta\theta\right)}, \tag{42}$$

and where the N-dimensional DFT vector $\boldsymbol{\psi}_{N,n}$ is defined for $N \in \mathbb{Z}^+$ and $n \in \mathbb{Z}$ as

$$\boldsymbol{\psi}_{N,n} \triangleq \frac{1}{\sqrt{N}}\left[1 \;\; e^{jn\frac{2\pi}{N}\cdot 1} \;\; \cdots \;\; e^{jn\frac{2\pi}{N}\cdot(N-1)}\right]^{\mathrm{T}}. \tag{43}$$

Proof: See Appendix A.□

From the decomposition in (41), we can verify (40) using the property $\sum_{n\in\mathbb{Z}} J_n^2(\beta) = 1$ and the fact that

$$\boldsymbol{\psi}_{N,n_1}^{\mathrm{H}}\boldsymbol{\psi}_{N,n_2} = \begin{cases} 1, & n_1 = n_2 + kN,\ k \in \mathbb{Z} \\ 0, & \text{otherwise} \end{cases}. \tag{44}$$

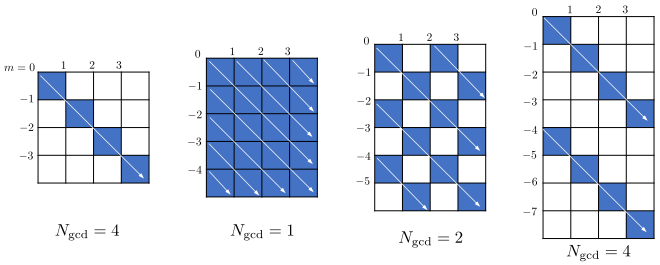

Fig. 3. Structure of the coupling coefficient matrix $\mathbf{Z} = \mathbf{W}_{N_r}^{\mathrm{H}}\mathbf{H}\mathbf{W}_{N_t}$ for $N_t = 4$, and $N_r = 4$, 5, 6, and 8. Nonzero entries can occur on the mth diagonal only if m is an integer multiple of N_{gcd}, as indicated by the arrows.

B. Coupling Coefficient Matrix Analysis

For an integer $N \in \mathbb{Z}^+$, the N-dimensional DFT matrix is defined as

$$\mathbf{W}_N \triangleq \left[\boldsymbol{\psi}_{N,0}\ \boldsymbol{\psi}_{N,1}\ \cdots\ \boldsymbol{\psi}_{N,N-1}\right] \in \mathbb{C}^{N\times N}. \tag{45}$$

It is clear that $\mathbf{W}_N$ is unitary, meaning $\mathbf{W}_N^{\mathrm{H}}\mathbf{W}_N = \mathbf{I}_N$. Now, let us define the $N_r \times N_t$ coupling matrix $\mathbf{Z}$ as

$$\mathbf{Z} \triangleq \mathbf{W}_{N_r}^{\mathrm{H}}\mathbf{H}\mathbf{W}_{N_t}. \tag{46}$$

If the input vector $\mathbf{x}$ in (39) is generated by performing N_t-dimensional DFT precoding on the information data symbols, and N_r-dimensional DFT combining is applied to $\mathbf{y}$, then $\mathbf{Z}$ represents the mapping between the data symbols and the combined receive signal. The element of $\mathbf{Z}$ at row $0 \le k_t \le N_t - 1$ and column $0 \le k_r \le N_r - 1$ is given by

$$\mathbf{Z}[k_r, k_t] = Z_{k_r,k_t} = \boldsymbol{\psi}_{N_r,k_r}^{\mathrm{H}}\mathbf{H}\boldsymbol{\psi}_{N_t,k_t}, \tag{47}$$

which constitutes the coupling coefficient between $\boldsymbol{\psi}_{N_t,k_t}$ and $\boldsymbol{\psi}_{N_r,k_r}$ through the channel $\mathbf{H}$. For this reason, $\mathbf{Z}$ is referred to as the coupling coefficient matrix for DFT precoding and combining.

In passing, we note that DFT precoding and combining are lossless, as clarified by the following lemma.

Lemma 1: Let $\mathbf{H} \in \mathbb{C}^{N_r\times N_t}$ be an arbitrary matrix, where $N_r \ge N_t$, and let $\mathbf{W}_N$ the N-point DFT matrix as defined in (45). Then $\mathbf{H}$ and $\mathbf{Z} = \mathbf{W}_{N_r}^{\mathrm{H}}\mathbf{H}\mathbf{W}_{N_t} \in \mathbb{C}^{N_r\times N_t}$ share the same singular values.

Proof: Since $\mathbf{W}_N$ is unitary, it follows that

$$\mathbf{Z}^{\mathrm{H}}\mathbf{Z} = \mathbf{W}_{N_t}^{\mathrm{H}}\mathbf{H}^{\mathrm{H}}\mathbf{H}\mathbf{W}_{N_t}.$$

Consequently, $\mathbf{Z}^{\mathrm{H}}\mathbf{Z}$ and $\mathbf{H}^{\mathrm{H}}\mathbf{H}$ have the same eigenvalues [33 p. 65,(9)], which implies the lemma.□

Remark 2: In our analysis, we have assumed an ideal reception of the electric field using $\mathcal{A}_r$. In practical scenarios where the received signal also contains a noise vector $\mathbf{n}$, comprising i.i.d. zero-mean complex Gaussian elements, Lemma 1 indicates that the channel capacity is not affected by DFT precoding and combining. This is because $\mathbf{W}_{N_r}^{\mathrm{H}}\mathbf{n}$ and $\mathbf{n}$ have the same statistical distribution.

In Theorem 3, we will formally demonstrate that the coupling coefficient matrix $\mathbf{Z}$ exhibits a multidiagonal structure. Specifically, the mth diagonal[7] of $\mathbf{Z}$ can contain nonzero

[7]The mth diagonal of $\mathbf{Z}$ refers to the elements $Z_{k,l}$ where $m = l - k$. Thus, the $m = 0$ diagonal is the main diagonal, and the $m > 0$ diagonals lie above the main diagonal. The valid range of m is from $1 - N_r$ to $N_t - 1$.

elements only if m is a multiple of $N_{\text{gcd}} = \gcd(N_t, N_r)$. Consequently, all other diagonals will consist solely of zero elements. This pattern is illustrated in Fig. 3, which shows four examples where $N_t = 4$ and $N_r = 4$, 5, 6, and 8, yielding $N_{\text{gcd}} = 4$, 1, 2, and 4, respectively. In these $N_r \times N_t$ grids, the blue cells indicate the positions of potentially nonzero elements.

Theorem 3: Consider the coupling coefficient matrix $\mathbf{Z}$ for an $N_t \times N_r$ UCA system with DFT precoding and combining, as defined in (46), where $N_r \geq N_t$. Let $N_{\text{gcd}} = \gcd(N_t, N_r)$ and $N_{\text{lcm}} = \text{lcm}(N_t, N_r)$. The elements along the mth diagonal of $\mathbf{Z}$ are

$$Z_{k_t-m,k_t} = \begin{cases} \sqrt{N_t N_r} \sum\limits_{n \in \mathcal{N}^*_{k_t,m}} J_n(\beta) e^{jn\left(\frac{\pi}{2}+\Delta\theta\right)}, & m \in N_{\text{gcd}}\mathbb{Z} \\ 0, & \text{otherwise} \end{cases}, \tag{48}$$

where Z_{k_r,k_t} is defined in (47), and

$$\mathcal{N}^*_{k_t,m} \triangleq k_t - mp_1 N_t / N_{\text{gcd}} + N_{\text{lcm}}\mathbb{Z}, \tag{49}$$

with (p_1, q_1) being the solution to the Diophantine equation $pN_t + qN_r = N_{\text{gcd}}$ obtained by the extended Euclidean algorithm.

Proof: See Appendix B.□

A few observation regarding the properties of the matrix $\mathbf{Z}$ are as follows.

- Each column of $\mathbf{Z}$ contains at most N_r/N_{gcd} nonzero elements, and each row contains at most N_t/N_{gcd} nonzero elements.
- In cases where $N_r = LN_t$ for some $L \in \mathbb{Z}^+$, it follows that $N_{\text{gcd}} = N_t$. This configuration results in $\mathbf{Z}$ being composed of L stacked diagonal $N_t \times N_t$ matrices. Essentially, each input mode experiences a $1 \times L$ single-input multiple-output (SIMO) channel to the output modes, eliminating any crosstalk between input modes.
- The elements on the mth diagonal, where $m \in N_{\text{gcd}}\mathbb{Z}$, are not necessarily nonzero. Since $\|\mathbf{Z}\|_{\text{F}}^2 = \|\mathbf{H}\|_{\text{F}}^2 = N_t N_r$, some coupling coefficients may be very small. As a general guideline, the parameter β should be sufficiently large to ensure that all elements are significant.

C. $N_t \times LN_tL$ UCA Channel Capacity Analysis

Theorem 3 demonstrates that DFT precoding and combining are particularly advantageous when $N_r = LN_t$, where $L \in \mathbb{Z}^+$. For this specific scenario, the singular values of the UCA channel matrix can be expressed as outlined in the following corollary to Theorem 3.

Corollary 1: For $L \in \mathbb{Z}^+$, the unsorted singular values of the $LN_t \times N_t$ UCA channel matrix $\mathbf{H}$ are given by

$$\sigma_{k_t} = \sqrt{LN_t^2 \sum_{l=0}^{L-1} \left| \sum_{n \in LN_t\mathbb{Z}} e^{jn\left(\frac{\pi}{2}+\Delta\theta\right)} J_{k_t+lN_t+n}(\beta) \right|^2}, \tag{50}$$

for $0 \leq k_t \leq N_t - 1$.

Proof: According to Lemma 1, the matrices $\mathbf{Z}^{\text{H}}\mathbf{Z}$ and $\mathbf{H}^{\text{H}}\mathbf{H}$ have the same eigenvalues. When $N_r = LN_t$, the matrix $\mathbf{Z}$ is composed of L stacked diagonal $N_t \times N_t$ matrices. As a result, $\mathbf{Z}^{\text{H}}\mathbf{Z}$ becomes an $N_t \times N_t$ real diagonal matrix, with its diagonal elements representing the eigenvalues of both $\mathbf{Z}^{\text{H}}\mathbf{Z}$ and $\mathbf{H}^{\text{H}}\mathbf{H}$. It can be readily verified that for $0 \leq k_t \leq N_t - 1$, $\sigma_{k_t}^2 \triangleq [\mathbf{Z}^{\text{H}}\mathbf{Z}]_{k_t,k_t}$ is expressed as

$$\sigma_{k_t}^2 = \sum_{k_r=0}^{N_r-1} \left| Z_{k_r,k_t} \right|^2 = \sum_{l=0}^{L-1} \left| Z_{k_t+lN_t,k_t} \right|^2, \tag{51}$$

and applying Theorem 3 directly, we find that

$$Z_{k_t+lN_t,k_t} = \sqrt{LN_t^2} \sum_{n \in k_t+lN_t+LN_t\mathbb{Z}} J_n(\beta) e^{jn\left(\frac{\pi}{2}+\Delta\theta\right)}. \tag{52}$$

We derive (50) by extracting the factor $e^{j(k_t+lN_t)\left(\frac{\pi}{2}+\Delta\theta\right)}$ from the sum in (52) and then substituting the result into (51).□

The following relation is valid for any values of β and $\Delta\theta$:

$$\sum_{k_t=0}^{N_t-1} \sigma_{k_t}^2 = \|\mathbf{H}\|_{\text{F}}^2 = \|\mathbf{Z}\|_{\text{F}}^2 = LN_t^2. \tag{53}$$

This equation indicates that the total channel gain, LN_t^2, is constant. However, the parameters β and $\Delta\theta$ determine the distribution of this total gain across the spatial subchannels within the UCA channel, as detailed in Corollary 1. It is noteworthy that there is an analogy between this equation and the expression for channel gain in (26).

Remark 3: In the special case where $N_r = N_t$, a scenario frequently explored in the literature, the square coupling coefficient matrix $\mathbf{Z}$ has nonzero elements exclusively on its main diagonal. This phenomenon arises from the fact that the channel matrix $\mathbf{H}$ becomes circulant, meaning that its element $\mathbf{H}[n_r, n_t]$ depends solely on $(n_r - n_t) \mod N_t$ (we refer to the discussion around [13, Eq. (22)]). In this case, the singular values are given by $\sigma_{k_t} = |Z_{k_t,k_t}|$ for $k_t = 0, 1, \ldots, N_t - 1$, and it follows directly from (52) that

$$Z_{k_t,k_t} = N_t \sum_{n \in k_t+N_t\mathbb{Z}} e^{jn\left(\frac{\pi}{2}+\Delta\theta\right)} J_n(\beta). \tag{54}$$

We previously examined this scenario in [1] with the additional assumption that $\Delta\theta = 0$. The expression derived for the eigenvalues in [1, Eq. (28)] coincides with (54) when $\Delta\theta = 0$. Comparing (54) with (47), it becomes evident that (54) provides deeper insights into how the singular values are affected by β and $\Delta\theta$. Finally, it is worth noting that if $N_t = N_r$ is even and $\Delta\theta = \pi/N_r$, then $\sigma_{N_t/2} = |Z_{N_t/2,N_t/2}| \equiv 0$ for all β. A proof of this statement can be found in Appendix C.

The UCA channel matrix $\mathbf{H}$ is energy-normalized similar to the linear operator A used for the CCA channel. For channel capacity analysis, we encounter challenges akin to those discussed in Section II-C. We reuse the notation G_{P} to denote that, when a single spatial subchannel with singular value σ is employed, one watt of transmit power will yield a receive signal power of $G_{\text{P}}\sigma^2$ watt. Additionally, we assume that independent, white, complex Gaussian noise with a power spectral density of N_0 watt per hertz is added to the received data signal post-combination. The system is considered narrow-band, with a bandwidth B hertz centered

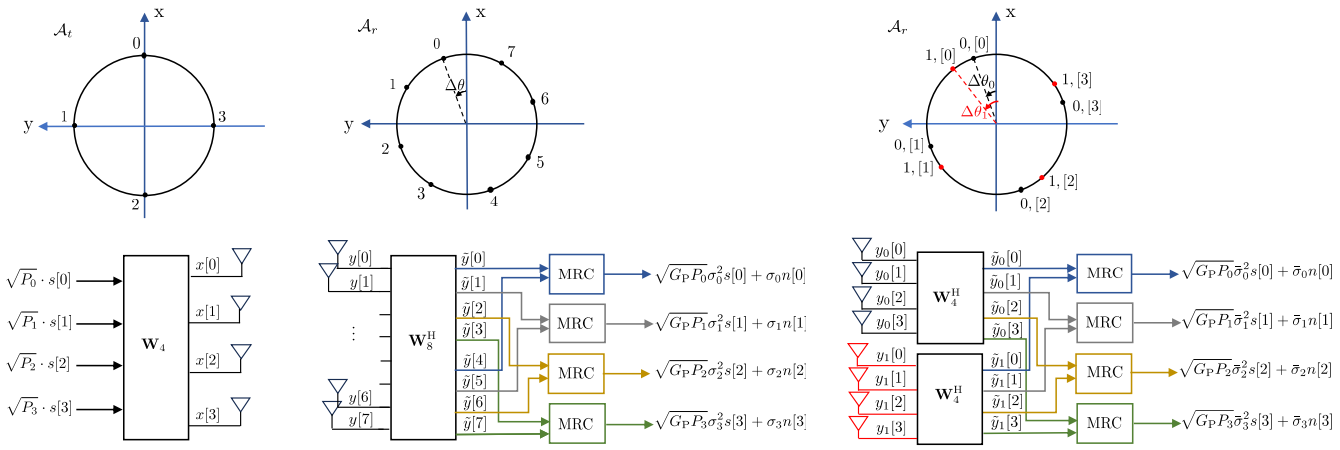

Fig. 4. Illustration of (a) the common transmitting structure, (b) Receiving Structure 1, and (c) Receiving Structure 2 with $N_t = 4$ and $L = 2$ ($N_r = 8$). In Receiving Structure 2, the antenna indexing is in the form of $l, [k_l]$, where $0 \le k_l \le N_t - 1$ indexes the antennas of the lth ($0 \le l \le L-1$) virtual UCA; and the antenna indexed by $l, [k_l]$ corresponds to the n_tth row of $\overline{\mathbf{H}}$, where $n_t \triangleq (lN_t + k_l)$. Note that in Receiving Structure 2, the physical antennas with indices $n_t = 0, 1, 2, \ldots$ are not placed sequentially on the circle. In the example shown in (c), the first virtual UCA (marked using black dots) consists of physical antennas with indices $n_t \in \{0, 1, 2, 3\}$, while the second (marked using red dots) consists of antennas with indices $n_t \in \{4, 5, 6, 7\}$. Each virtual UCA resolves a copy of all four data streams.

around $\omega/2\pi$ (where $B \ll \omega/2\pi$). Consequently, we arrive at the familiar input-output relationship

$$\mathbf{y} = \sqrt{G_{\mathrm{P}}}\mathbf{H}\mathbf{x} + \mathbf{n}, \tag{55}$$

where $\mathbf{n} \sim \mathcal{CN}(\mathbf{0}, N_0\mathbf{I}_{LN_t})$. It is assumed that the channel state information is available at both the transmitter and the receiver. The Shannon channel capacity, subject to a total transmit power constraint P_{T}, is therefore expressed as

$$C_{\mathrm{UCA}} = B\sum_{k_t=0}^{N_t-1} \log_2\left(1 + \frac{P_{k_t} G_{\mathrm{P}} \sigma_{k_t}^2}{N_0 B}\right) \quad [\text{bit/s}]. \tag{56}$$

where P_{k_t} for $k_t = 0, 1, \ldots, N_t - 1$ is determined through water-filling power allocation.

IV. Optimal Spatial Multiplexing Transceiver Structures

Building on Section III, we explore two optimal transceiver structures that utilize DFT precoding and combining for spatial multiplexing in an $N_t \times LN_t$ LOS MIMO system with circular arrays, aiming to achieve high data rate radio links. Both structures share an identical transmitting design but differ in their array configurations and combining strategies at the receiver. The second structure incorporates a non-UCA receiving array, resulting in a distinct channel matrix $\overline{\mathbf{H}}$, in contrast to the UCA channel matrix $\mathbf{H}$. When specifying the number of receive antennas and angular offset for a UCA channel, we use the notation $(N_r, \Delta\theta)$ appended to $\mathbf{H}$ and the coupling coefficient matrix $\mathbf{Z}$.

A. Transmitting Structure

The transmitting structure employs N_t-dimensional DFT precoding, as illustrated in Fig. 4(a) using $N_t = 4$ as an example. The transmitted signal vector $\mathbf{x}$ is given by

$$\mathbf{x} = \mathbf{W}_{N_t}\mathbf{P}^{1/2}\mathbf{s}, \tag{57}$$

where $\mathbf{s} = (s[0], s[1], \ldots, s[N_t - 1])^{\mathrm{T}}$ contains independent data symbols with $E\{|s[k_t]|^2\} = 1$ for all $0 \le k_t \le N_t - 1$. The matrix $\mathbf{P} \triangleq \mathrm{diag}\left(P_0, P_1, \ldots, P_{N_t-1}\right)$ represents the power allocation across the subchannels, with $\sum_{k_t=0}^{N_t-1} P_{k_t} = P_{\mathrm{T}}$, where P_{T} is the total transmit power. The setup ensures that $E\{\|\mathbf{x}\|^2\} = P_{\mathrm{T}}$.

The received signal vector follows the expression in (55), with $\mathbf{H}$ replaced by $\overline{\mathbf{H}}$ for the second structure. The system is again narrow-band, with bandwidth B hertz centered around the frequency $\omega/2\pi$. In the context of LOS radio links for high data rate transmission in high SNR regimes, we assume the use of high-gain antennas. The transmit G_t and receive G_r antenna gains are consolidated into G_{P} to streamline the analysis[8]. This approach enables us to focus on the reference SNR $\mathrm{SNR}_0(P_{\mathrm{T}})$, as defined in (32), in our channel capacity discussions.

B. Receiving Structure 1: Ln_t-Element UCASingle UCA

The first receiving structure, illustrated in Fig. 4(b), comprises $N_r = LN_t$ antenna elements arranged in a single UCA with an angular offset of $\Delta\theta$, see (34). The channel matrix for this configuration is represented by $\mathbf{H}(LN_t, \Delta\theta)$. An LN_t-dimensional DFT combining is performed to the received signal vector $\mathbf{y}$, resulting in

$$\tilde{\mathbf{y}} = \mathbf{W}_{LN_t}^{\mathrm{H}}\mathbf{y} = \sqrt{G_{\mathrm{P}}}\mathbf{Z}(LN_t, \Delta\theta)\mathbf{P}^{1/2}\mathbf{s} + \tilde{\mathbf{n}} \tag{58}$$

where $\tilde{\mathbf{n}} = \mathbf{W}_{LN_t}^{\mathrm{H}}\mathbf{n} \sim \mathcal{CN}(\mathbf{0}, N_0\mathbf{I}_{LN_t})$.

From the multidiagonal structure of $\mathbf{Z}(LN_t, \Delta\theta)$, we know that each transmitted data symbol experiences an interference-free $1 \times L$ SIMO channel, with the complex channel gains provided in (52). The L received copies are combined

[8]Given $D \gg \max(R_t, R_r)$, the directional variation between different transmit and receive antenna pairs can be neglected, allowing for maximum antenna gains G_t and G_r to be achieved across all antenna pairs.

according to the maximum ratio combining (MRC) policy through the following operation:

$$\check{\mathbf{y}} = \mathbf{Z}^{\mathrm{H}}\tilde{\mathbf{y}} = \sqrt{G_{\mathrm{P}}}\mathbf{Z}^{\mathrm{H}}\mathbf{Z}\mathbf{P}^{1/2}\mathbf{s} + \check{\mathbf{n}}, \tag{59}$$

where $\check{\mathbf{n}} = \mathbf{Z}^{\mathrm{H}}\tilde{\mathbf{n}} \sim \mathcal{CN}(0, N_0\mathbf{Z}^{\mathrm{H}}\mathbf{Z})$. As discussed in Section III-C, $\mathbf{Z}^{\mathrm{H}}\mathbf{Z}$ is an $N_t \times N_t$ real diagonal matrix, with its diagonal elements being the squares of the unsorted singular values of $\mathbf{H}(LN_t, \Delta\theta)$ as given in (50). Thus, for each transmitted data symbol

$$\check{y}[k_t] = \sqrt{G_{\mathrm{P}}P_{k_t}}\sigma_{k_t}^2 s[k_t] + \sigma_{k_t} n[k_t], \quad 0 \le k_t \le N_t - 1,$$

where $n[k_t] \sim \mathcal{CN}(0, N_0)$. The received SNR for the k_tth symbol is therefore given by

$$\mathrm{SNR}_{k_t} = \frac{G_{\mathrm{P}}P_{k_t}}{N_0 B}\sigma_{k_t}^2 = \frac{P_{k_t}}{P_{\mathrm{T}}}\mathrm{SNR}_0(P_{\mathrm{T}})\sigma_{k_t}^2. \tag{60}$$

It is clear the channel capacity given by (56) can be achieved.

C. Receiving Structure 2: L Virtual N_t-Element UCAssubUCA

The second receiving structure, depicted in Fig. 4(c), organizes the LN_t antenna elements into L groups, each containing N_t antennas that form a *virtual UCA* with an angular offset $\Delta\theta_l \in [0, 2\pi/N_t)$, $0 \le l \le L-1$. Specifically, the lth virtual UCA comprises N_t receive antennas positioned at angles given by

$$\theta_{l,n_r} = \frac{2\pi}{N_t}n_r + \Delta\theta_l, \qquad 0 \le n_r \le N_t. \tag{61}$$

The $LN_t \times N_t$ channel matrix, $\overline{\mathbf{H}}$, is constructed by vertically stacking $\mathbf{H}(N_t, \Delta\theta_l)$ for each group. Notably, the uniform arrangement in Receiving Structure 1 is a special case of this setup, occurring when $\Delta\theta_l = 2l\pi/N_r$. In this scenario, rearranging the rows of $\overline{\mathbf{H}}$ yields $\mathbf{H}(LN_t, \Delta\theta_0)$.

For simplicity, we define $\mathbf{H}_l = \mathbf{H}(N_t, \Delta\theta_l)$ and $\mathbf{Z}_l = \mathbf{Z}(N_t, \Delta\theta_l)$, where $\mathbf{Z}_l$ have nonzero elements only on its main diagonal (see noted in Remark 3). Since each $\mathbf{H}_l$ is circulant, it follows that $\overline{\mathbf{H}}$ is block-circulant, allowing it to be diagonalized using DFT-matrices. It follows that

$$\mathbf{W}_{N_t}^{\mathrm{H}}\overline{\mathbf{H}}^{\mathrm{H}}\overline{\mathbf{H}}\mathbf{W}_{N_t} = \mathbf{W}_{N_t}^{\mathrm{H}}\left(\sum_{l=0}^{L-1}\mathbf{H}_l^{\mathrm{H}}\mathbf{H}_l\right)\mathbf{W}_{N_t} = \sum_{l=0}^{L-1}\mathbf{Z}_l^{\mathrm{H}}\mathbf{Z}_l,$$

indicating that $\overline{\mathbf{H}}^{\mathrm{H}}\overline{\mathbf{H}}$ and $\sum_{l=0}^{L-1}\mathbf{Z}_l^{\mathrm{H}}\mathbf{Z}_l$ share the same eigenvalues, which are simply the diagonal elements of the latter. We denote these eigenvalues as $\bar{\sigma}_0^2, \bar{\sigma}_1^2, \ldots, \bar{\sigma}_{N_t-1}^2$. It can be verified, using either (50) (with $N_r = N_t$) or (54), that

$$\bar{\sigma}_{k_t} = \sqrt{N_t^2\sum_{l=0}^{L-1}\left|\sum_{n\in N_t\mathbb{Z}} e^{jn\left(\frac{\pi}{2}+\Delta\theta_l\right)}J_{k_t+n}(\beta)\right|^2}, \tag{62}$$

for $0 \le k_t \le N_t - 1$. Additionally, we have that

$$\sum_{k_t=0}^{N_t-1}\bar{\sigma}_{k_t}^2 = \|\overline{\mathbf{H}}\|_{\mathrm{F}}^2 = LN_t^2. \tag{63}$$

The analysis above suggests the following receiving strategy: Perform N_t-dimensional DFT combining to each virtual UCA, resolving a copy for each transmitted symbol. At the lth virtual UCA, the received signal vector is $\mathbf{y}_l = \sqrt{G_{\mathrm{P}}}\mathbf{H}_l\mathbf{x} + \mathbf{n}_l$, where $\mathbf{n}_l \sim \mathcal{N}(\mathbf{0}, N_0\mathbf{I}_{N_t})$. The DFT combining results in $\tilde{\mathbf{y}}_l = \sqrt{G_{\mathrm{P}}}\mathbf{Z}_l\mathbf{P}^{1/2}\mathbf{s} + \tilde{\mathbf{n}}_l$, where $\tilde{\mathbf{n}}_l = \mathbf{W}_{N_t}^{\mathrm{H}}\mathbf{n}_l \sim \mathcal{N}(\mathbf{0}, N_0\mathbf{I}_{N_t})$. This process yields L crosstalk-free copies for each transmitted data symbol, each experiencing different gains as specified by the diagonal elements of $\mathbf{Z}_l$. The L copies are then combined using the MRC policy, resulting in

$$\bar{\mathbf{y}} = \sum_{l=0}^{L-1}\mathbf{Z}_l^{\mathrm{H}}\tilde{\mathbf{y}}_l = \sqrt{G_{\mathrm{P}}}\left(\sum_{l=0}^{L-1}\mathbf{Z}_l^{\mathrm{H}}\mathbf{Z}_l\right)\mathbf{P}^{1/2}\mathbf{s} + \bar{\mathbf{n}}, \tag{64}$$

where $\bar{\mathbf{n}} = \sum_{l=0}^{L-1}\mathbf{Z}_l^{\mathrm{H}}\tilde{\mathbf{n}}_l \sim \mathcal{N}\left(0, N_0\sum_{l=0}^{L-1}\mathbf{Z}_l^{\mathrm{H}}\mathbf{Z}_l\right)$. Thus, each symbol can be written as

$$\bar{y}[k_t] = \sqrt{G_{\mathrm{P}}P_{k_t}}\bar{\sigma}_{k_t}^2 s[k_t] + \bar{\sigma}_{k_t} n[k_t], \quad 0 \le k_t \le N_t - 1,$$

where $n[k_t] \sim \mathcal{CN}(0, N_0)$. The received SNR for the k_tth symbol is

$$\overline{\mathrm{SNR}}_{k_t} = \frac{G_{\mathrm{P}}P_{k_t}}{N_0 B}\bar{\sigma}_{k_t}^2 = \frac{P_{k_t}}{P_{\mathrm{T}}}\mathrm{SNR}_0(P_{\mathrm{T}})\bar{\sigma}_{k_t}^2 \tag{65}$$

The Shannon capacity of this channel, given by (56) with $\sigma_{k_t}^2$ replaced by $\bar{\sigma}_{k_t}^2$, can be achieved.

D. Ellipticity as a Performance Metric

The two structures differ in receiver antenna placement and subsequent combining. As (53) and (63) show, they have the same sum of squared singular values. However, the singular values are distributed different over the spatial channels. Since the first structure is a special case of the second, the latter is expected to perform as well as or better than the former when optimized angular offsets are applied. Given our focus on high data rate radio link applications in the high SNR regime, we use the ellipticity statistic [34] as a proxy for channel capacity when comparing performance, which is defined as

$$\zeta(\mathbf{H}) = m_g(\mathbf{H})/m_a(\mathbf{H}), \tag{66}$$

where $m_g(\mathbf{H})$ and $m_a(\mathbf{H})$ represent the geometric mean and arithmetic mean of the squared singular values, respectively, i.e.,

$$m_g(\mathbf{H}) \triangleq \sqrt[N_t]{\prod_{k_t=0}^{N_t-1}\sigma_{k_t}^2}, \quad m_a(\mathbf{H}) \triangleq \frac{1}{N_t}\sum_{k_t=0}^{N_t-1}\sigma_{k_t}^2. \tag{67}$$

The name 'ellipticity' comes from the fact that $\zeta(\mathbf{H})$ represents the ellipticity of the hyperellipsoid defined by the squared singular values as its axis lengths. Clearly, $\zeta(\mathbf{H}) \le 1$, with equality if and only if all singular values are equal. Moreover, $\zeta(\mathbf{H}) \ge 0$, with equality holding when one or several singular values are zero, i.e., when the channel matrix is not full rank.

When $\mathrm{SNR}_0(P_{\mathrm{T}})\sigma_{k_t}^2/N_t \gg 1$ for all k_t, i.e., when the SNR is high and the channel matrix has full rank, equal power allocation (EPA) is near-optimal. The channel capacity is, under these conditions, approximately equal to

$$C_{\mathrm{EPA}} = B\sum_{k_t=0}^{N_t-1}\log_2\left(1 + \frac{\mathrm{SNR}_0(P_{\mathrm{T}})}{N_t}\sigma_{k_t}^2\right) \tag{68}$$

$$\approx B\sum_{k_t=0}^{N_t-1}\log_2\left(\frac{\mathrm{SNR}_0(P_{\mathrm{T}})}{N_t}\sigma_{k_t}^2\right) \tag{69}$$

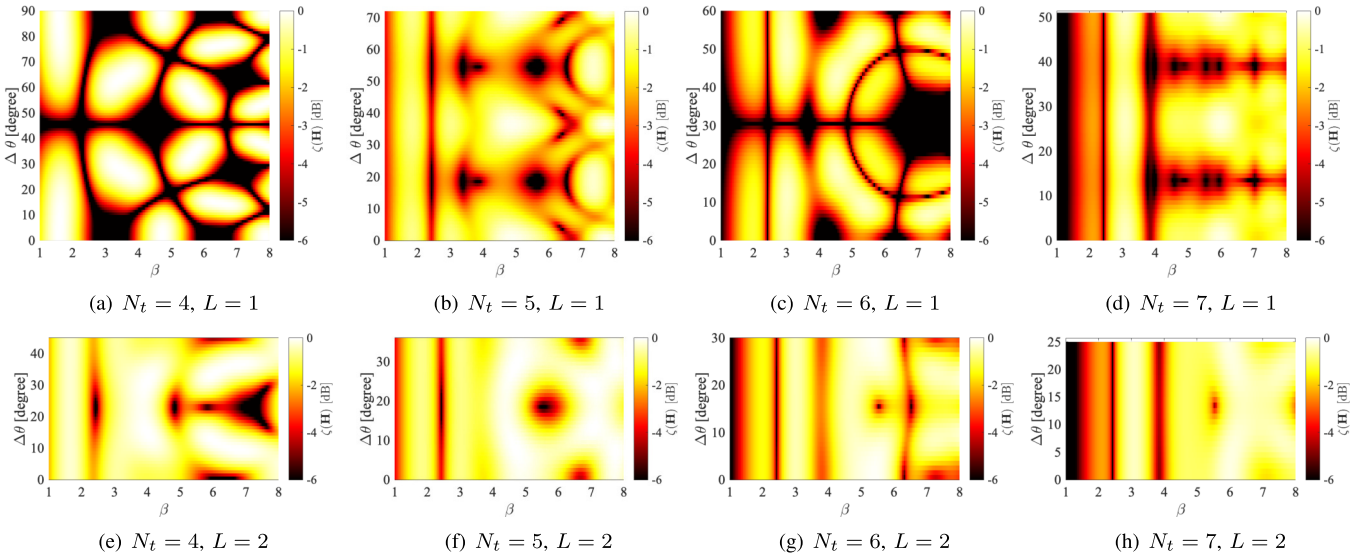

(a) $N_t = 4,\ L = 1$ (b) $N_t = 5,\ L = 1$ (c) $N_t = 6,\ L = 1$ (d) $N_t = 7,\ L = 1$

(e) $N_t = 4,\ L = 2$ (f) $N_t = 5,\ L = 2$ (g) $N_t = 6,\ L = 2$ (h) $N_t = 7,\ L = 2$

Fig. 5. Ellipticity performance of the UCA channel as β vary in $[1, 8]$ and $\Delta\theta$ vary in $[0, 2\pi/LN_t)$ (shown in degrees). Bright areas indicate good ellipticity performance (close to 0), while dark areas indicate poor ellipticity performance.

$$= BN_t \log_2\left(\frac{\mathrm{SNR}_0(P_\mathrm{T})}{N_t} m_g(\mathbf{H})\right) \tag{70}$$

$$= BN_t \log_2\left(\frac{\mathrm{SNR}_0(P_\mathrm{T})}{N_t} m_a(\mathbf{H})\right) + BN_t \log_2\left(\zeta(\mathbf{H})\right). \tag{71}$$

The first term in (71) is the maximum achievable rate in the full-rank, high SNR regime when all singular values are equal, i.e., when $\sigma_{k_t}^2 = m_a(\mathbf{H})$. Hence, the second term in (71), which is always non-positive, is the penalty due to singular value dispersion. Put differently, $\zeta(\mathbf{H})$, expressed in dB, quantifies the SNR penalty per spatial subchannel due to singular value dispersion in the high-SNR, full rank scenario. Clearly, the penalty term is zero when all singular values are equal, since $\zeta(\mathbf{H}) = 1$ in this case. A low $\zeta(\mathbf{H})$ indicates substantial singular value dispersion. However, in the extreme case when the channel matrix is not full rank, $\zeta(\mathbf{H}) = 0$ and the above analysis is not valid since the approximation (69) does not hold. Hence, $\zeta(\mathbf{H}) = 0$ does not imply zero channel capacity, but only loss of one or several spatial DOFs. Nevertheless, with this caveat in mind, ellipticity is a useful measure of singular value dispersion penalty for the high-SNR, full rank scenario.

V. Numerical Study

This paper extends the findings from [1], which investigated an $N_t \times N_t$ UCA channel with zero angular offset ($\Delta\theta = 0$). In the numerical study section of [1], we compared the performance of the UCA channel under this condition to that of a LOS MIMO channel using optimally designed ULAs. In our current study, we focus on an $N_t \times N_r$ discrete channel, where $N_r = LN_t$, $L = 1$ or 2, exploring various antenna placements and angular offsets. For convenience, we refer to the channels associated with Receiving Structure 1 and Receiving Structure 2 as the *UCA channel* and *nonUCA channel*, respectively.

A. Ellipticity Performance Evaluation

Fig. 5 presents color maps of $\zeta(\mathbf{H})$ (in dB) for the UCA channel under various settings ($4 \le N_t \le 7$, $L = 1, 2$), over the ranges $\beta \in [1, 8]$ and $\Delta\theta \in [0, 2\pi/N_r]$. Dark areas indicate low ellipticity (poor performance), while bright areas suggest values near 0 dB (good performance). The color maps reveal distinct patterns of $\zeta(\mathbf{H})$ for different settings, with a common mirror symmetry around $\Delta\theta = \pi/N_r$. This mirror symmetry arises because the ellipticity is an even function of $\Delta\theta$ and is periodic with period $2\pi/N_r$. These two properties are easily seen from the geometry of the antenna arrangement. A formal proof would show that the channel matrices $\mathbf{H}(\Delta\theta + k2\pi/N_r)$ and $\mathbf{H}(-\Delta\theta)$ can be obtained from $\mathbf{H}(\Delta\theta)$ through appropriate permutations of rows and columns, which effectively change the indexing of the antennas, but not the singular values. Hence, the ellipticity is the same for all three matrices, which proves periodicity and evenness. A complete derivation is omitted here due to lack of space. For all N_t, increasing L from 1 to 2 eliminates many dark areas. As noted in Remark 3, if $N_t = N_r$ is even and $\Delta\theta = \pi/N_r$, then $\sigma_{N_t/2} \equiv 0$ for all β), leading to a dark horizontal line at $\Delta\theta = \pi/N_r$ in Fig. 5(a) and Fig. 5(c). Corollary 1 predicts dark regions around $\beta \approx 2.4$ in all subfigures. According to (50), σ_0 depends on the phase-shifted sums of $J_{n\in N_t\mathbb{Z}}(\beta)$. Since $J_0(\beta) = 0$ when $\beta \approx 2.4$, and $J_{n\in N_t\mathbb{Z}, n\neq 0}(\beta) \approx 0$ for small β and large N_t, $\sigma_0 \approx 0$ for all $\Delta\theta$ when $\beta = 2.4$. Notably, increasing β does not always enhance $\zeta(\mathbf{H})$. Recall that $2(\beta + 1)$ estimates the number of effective DOFs of the CCA channel for large β. For $\beta \approx \beta_\mathrm{th} \triangleq (N_t - 1)/2$, bright regions appear for some $\Delta\theta$ in all subfigures. However, further increasing β may lead to dark regions for all $\Delta\theta$, as seen in Fig. 5(d), where $\beta_\mathrm{th} = 3$ and a dark region emerges at $\beta \approx 3.8$.

Fig. 6 presents color maps of $\zeta(\overline{\mathbf{H}})$ for the nonUCA channel with $N_t = 5, 6$ and $L = 2$, over the ranges $\beta \in [1, 8]$ and $\Delta\theta_0 \in [0, \pi/N_t)$, for five values of $\Delta\theta_\mathrm{diff} \triangleq \Delta\theta_1 - \Delta\theta_0$ within $[0, \pi/N_t]$. Choosing $\Delta\theta_\mathrm{diff} = 0$ theoretically offers twice the power gain

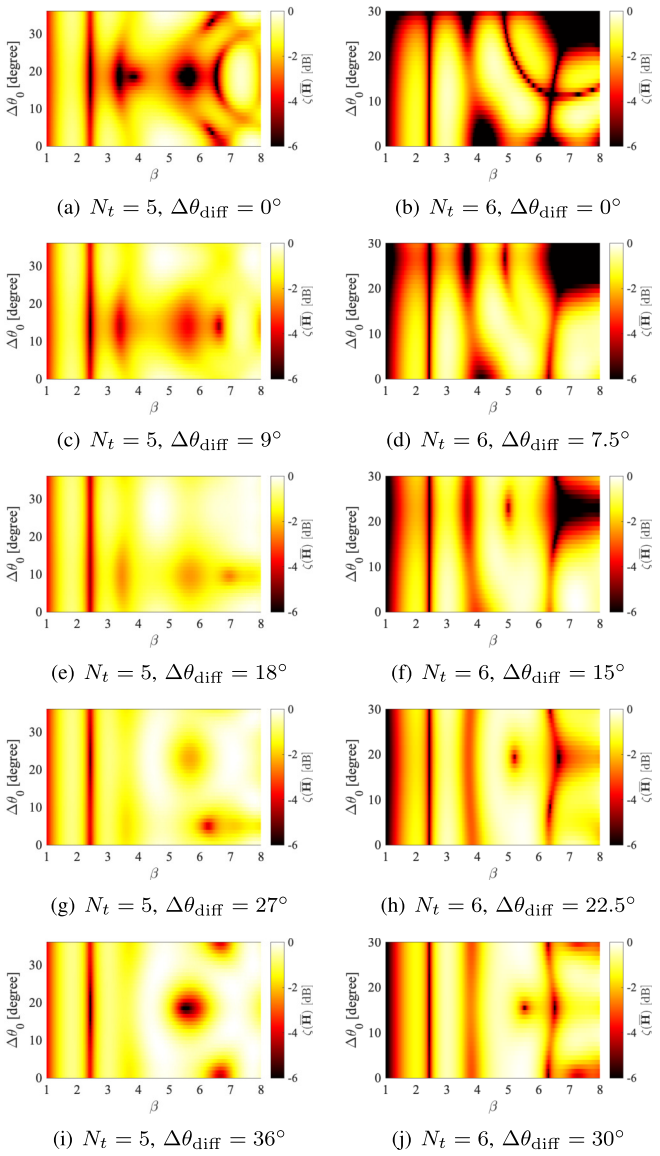

Fig. 6. Ellipticity performance of the nonUCA channel ($L = 2$) as β vary in $[1, 8]$ and $\Delta\theta_0$ vary in $[0, 2\pi/LN_t]$, with $\Delta\theta_{\text{diff}} \triangleq \Delta\theta_1 - \Delta\theta_0$ set to five equally spaced values between 0 and $2\pi/LN_t$.

of an $N_t \times N_t$ UCA channel, although this is impractical due to antenna overlap. On the other hand, setting $\Delta\theta_{\text{diff}} = \pi/N_t$ results in an $N_t \times 2N_t$ UCA configuration. As $\Delta\theta_{\text{diff}}$ increases, the ellipticity pattern transitions from an $N_t \times N_t$ to an $N_t \times 2N_t$ UCA channel, as observed in Fig. 6. The nonUCA channel can be advantageous for $N_t = 5$, as certain values of $\Delta\theta_{\text{diff}}$ (e.g., $\Delta\theta_{\text{diff}} = 18°$ and $27°$) reduce dark areas, indicating improved performance. However, this advantage is not as pronounced for $N_t = 6$.

Fig. 7 shows the ellipticity range over β for both UCA and nonUCA channels, corresponding to the settings in Fig. 5(b), (c), (f), (g) and Fig. 6(e), (h), respectively. The light yellow region represents the ellipticity of the nonUCA channel as $(\Delta\theta_0, \Delta\theta_1)$ varies over all combinations in the range $[0, 2\pi/N_t] \times [0, 2\pi/N_t]$. The variation in UCA ellipticity, as $\Delta\theta$ changes within $[0, 2\pi/N_t]$, is shown in purple or brown and is contained within the yellow nonUCA region. The nonUCA ellipticity plotted in green, with $\Delta\theta_0$ varying within $[0, 2\pi/N_t)$ and $\Delta\theta_{\text{diff}}$ held constant, is also encompassed in the yellow region. This behavior is understood from the analysis in Sec. IV. The results show that while adjusting $\Delta\theta$, the $N_t \times N_t$ UCA channel does not always achieve optimal ellipticity and can degrade to the worst performance. Conversely, the $N_t \times 2N_t$ UCA channel approaches optimal performance and avoids severe degradation for most β values. The nonUCA channel with fixed $\Delta\theta_{\text{diff}}$ show reduced variation across different β ranges, as demonstrated in Fig. 7(c) and (f). For applications such as LOS radio links, minimal variation over a wide range centered around the designed $(\beta, \Delta\theta)$ values is desirable to mitigate parameter drifts.

B. Singular Value and Channel Capacity

To gain deeper insights into channel behavior, we examine the singular values and channel capacity performances under various selected simulation settings.

Fig. 8 displays the best- and worst-case squared singular values for UCA and nonUCA channels under the same six settings as in Fig. 7, with β set to 3 and 5.5. 'Best' and 'worst' refer to scenarios maximizing or minimizing ellipticity by adjusting $\Delta\theta$ or $\Delta\theta_0$. A grid search is adopted to find $\Delta\theta_{\max}$, $\Delta\theta_{\min}$, $\Delta\theta_{0,\max}$, and $\Delta\theta_{0,\min}$ within their range using $0.1°$ steps. These best or worst angular offset values, while not unique as one can expect from the ellipticity color map symmetry, lead to the same singular value distribution. We choose those closest to 0 for legend display. As anticipated, $\Delta\theta_{\max}$ and $\Delta\theta_{0,\max}$ result in more uniform singular values closer to the reference line at $\sigma_k^2 = N_r$, while $\Delta\theta_{\min}$ and $\Delta\theta_{0,\min}$ yield zero or near-zero singular values, which corresponds to very low ellipticity values and reflects a loss of spatial DOF. Additionally, in Fig. 8(b) and (e), similar singular value distributions occur for the $N_t \times 2N_t$ UCA with $\beta = 3$ using both $\Delta\theta_{\max}$ and $\Delta\theta_{\min}$. Fig. 7(b) and (e) show that the resulting ellipticity values are nearly identical, indicating minimal impact from angular misalignment under these settings. Notably, $\Delta\theta = 0$ is sometimes the best choice for the UCA channel. This occurs in Fig. 8(a) for $\beta = 3$ and $\beta = 5.5$, Fig. 8(b) for $\beta = 3$, and Fig. 8(e) for $\beta = 5.5$, where $\Delta\theta_{\max} = 0$. These results are consistent with expectations from Fig. 5.

We also verified the derived singular value expressions through full-wave EM simulations using the same geometric configurations with half-wave strip dipole antennas. We utilized an in-house developed method of moments (MoM) code, which employs the Galerkin method to solve the electric field integral equation using Rao-Wilton-Glisson (RWG) basis [35]. The simulations were conducted at an operating frequency of 70 GHz, with a communication distance D is 1 km. The transmitter and receiver radii $R_t = R_r$ were set to 1.43 or 1.94 meters, corresponding to $\beta = 3$ or 5.5 (calculated using $R_t = R_r = \sqrt{D\lambda\beta/2\pi}$). The half-wave strip dipole antennas were orientated in the x-direction and positioned at the specified angular offsets. The EM simulations accounted for antenna mutual coupling and embedded element patterns, producing the full antenna system S-matrix. Singular values were obtained via SVD of the channel matrix and normalized so that the sum of their squares equals LN_t^2 (see (53) and

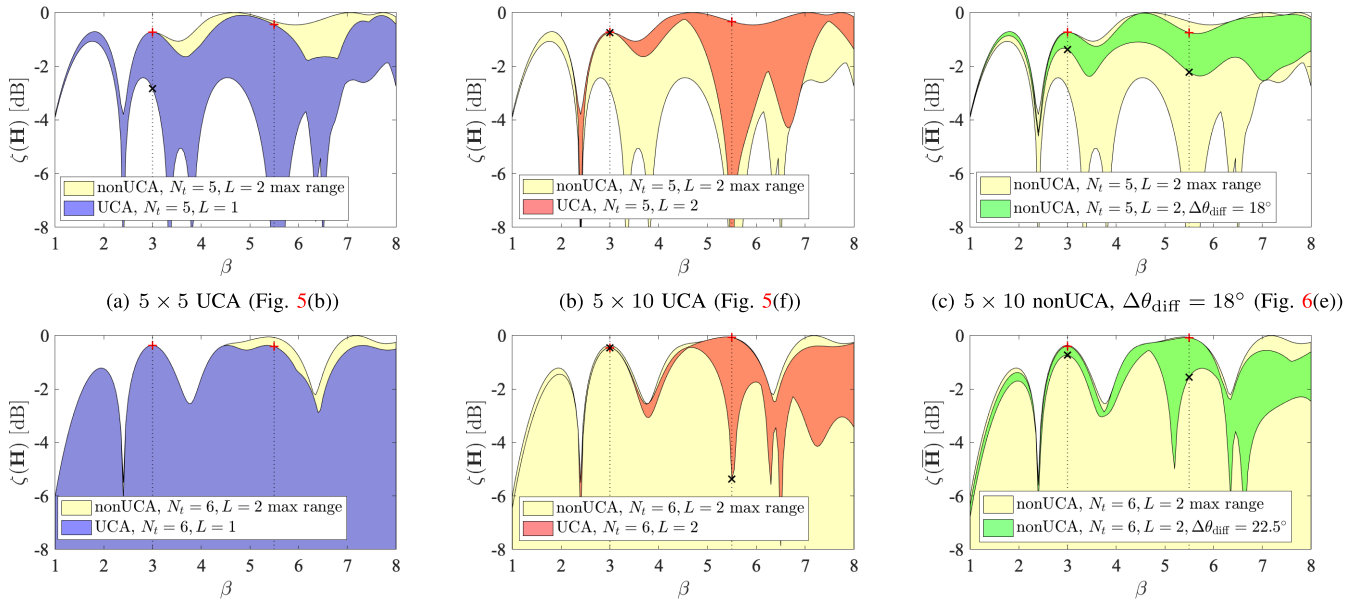

(a) 5×5 UCA (Fig. 5(b)) (b) 5×10 UCA (Fig. 5(f)) (c) 5×10 nonUCA, $\Delta\theta_{\text{diff}} = 18°$ (Fig. 6(e))

(d) 6×6 UCA (Fig. 5(c)) (e) 6×12 UCA (Fig. 5(g)) (f) 6×12 nonUCA, $\Delta\theta_{\text{diff}} = 22.5°$ (Fig. 6(h))

Fig. 7. Ellipticity variation ranges due to $\Delta\theta$ (for the UCA channel) or $\Delta\theta_0$ (for nonUCA channel) corresponding to six settings in Fig. 5 and Fig. 6. Note that the maximum variation range does not have a lower boundary in subplots (d)-(f), because the minimum ellipticity is zero for an even N_t. For $\beta = 3$ and $\beta = 5.5$, the maximum and minimum ellipticity are marked using red + and black $\times$.

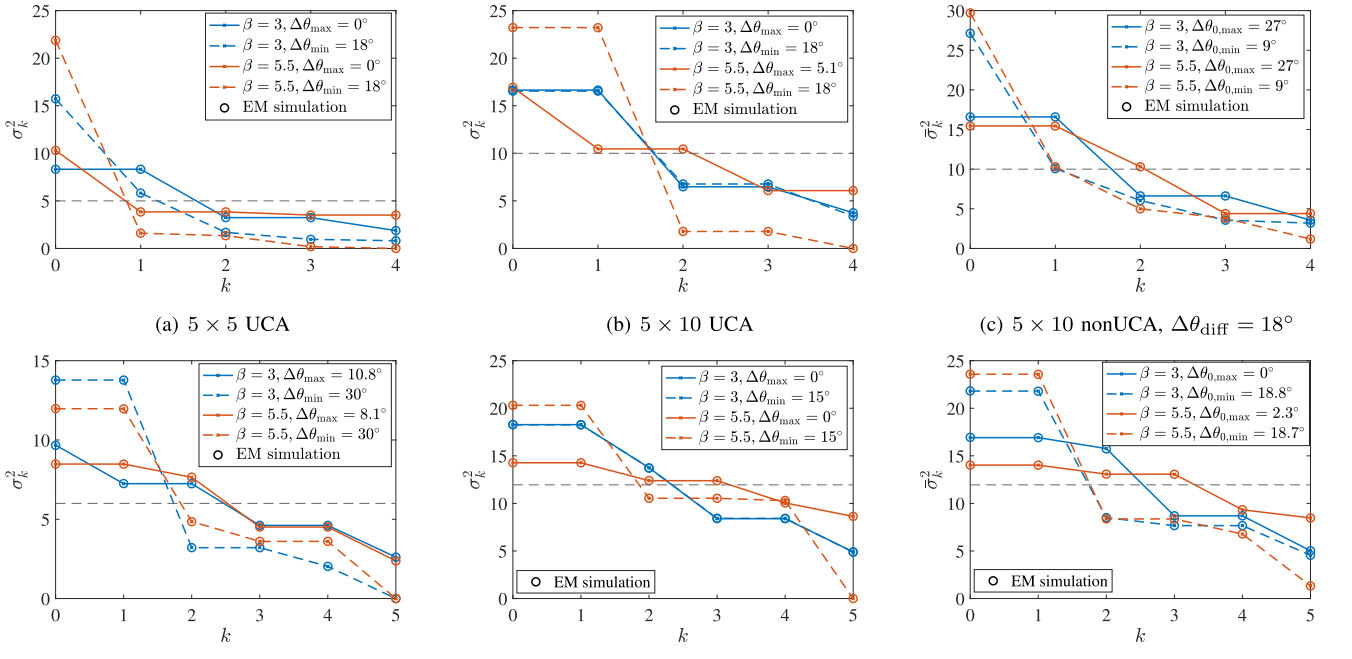

(a) 5×5 UCA (b) 5×10 UCA (c) 5×10 nonUCA, $\Delta\theta_{\text{diff}} = 18°$

(d) 6×6 UCA (e) 6×12 UCA (f) 6×12 nonUCA, $\Delta\theta_{\text{diff}} = 22\ 5°$

Fig. 8. The best and worst sets of singular values achieved at $\beta = 3$ and $\beta = 5.5$ by $\Delta\theta_{\max}$ (or $\Delta\theta_{0,\max}$) and $\Delta\theta_{\min}$ (or $\Delta\theta_{0,\min}$) under the same settings of Fig. 7. A dashed horizontal line at $\sigma_k^2 = N_r$ is plotted for reference.

(63)). The results, indicated by circular markers in Fig. 8, show good agreement with the analytical predictions, confirming the validity of the analysis[9].

[9]Note that the conditions in Section II-A must be satisfied to ensure the analysis's accuracy. In [1, Fig. 4], we demonstrated that discrepancies between EM simulation and analytical results can arise if these conditions are not met.

Fig. 9 compares the channel capacity performance for $N_t = 6$ and three β values. We access $N_t \times N_t$ and $N_t \times 2N_t$ UCA channels with $\Delta\theta_{\max}$ and $\Delta\theta_{\min}$, and the $N_t \times 2N_t$ nonUCA channel with the best angular offsets $(\Delta\theta_0, \Delta\theta_1)_{\max}$, determined via a grid search with a $0.1°$ step to maximize $\zeta(\overline{\mathbf{H}})$. Capacity curves are plotted against $\text{SNR}_0(P_T/N_t)$ over the range of $[-10, 40]$ dB, using water-filling power allocation. Singular

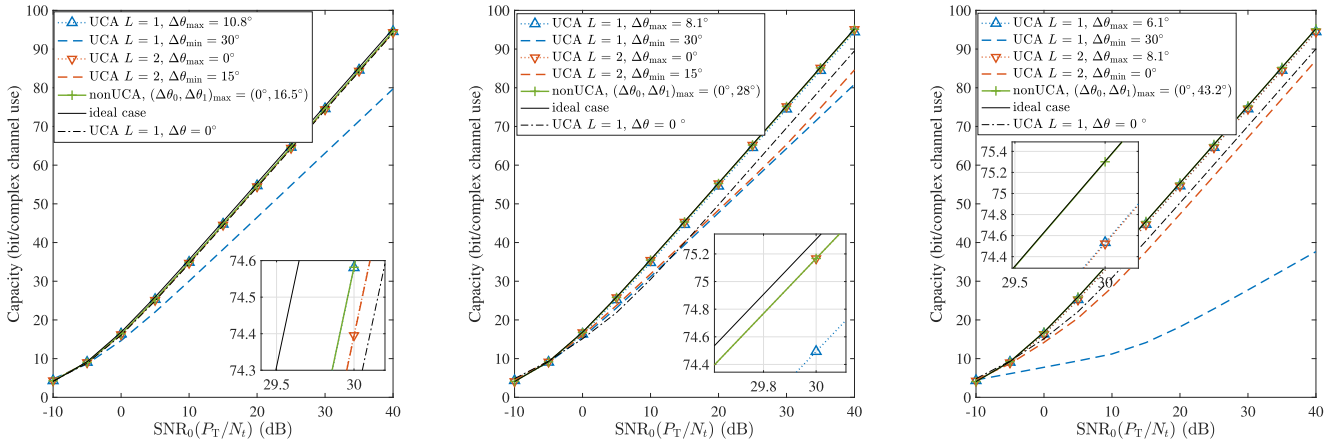

(a) $N_t = 6$, $\beta = 3$ (b) $N_t = 6$, $\beta = 5.5$ (c) $N_t = 6$, $\beta = 7.2$

Fig. 9. Capacity performance of best- and worse-case UCA and nonUCA channels for $N_t = 6$ and $\beta = 3$, 5.5, and 7.2, over the range $\mathrm{SNR}_0(P_\mathrm{T}/N_t) \in [-10, 40]$ dB.

values for channels with $2N_t$ receive antennas are down-scaled by $1/\sqrt{2}$ to isolate the singular value distribution effects from the power gain. After scaling, the worst-case capacity of the $N_t \times 2N_t$ nonUCA channel is identical to that of the $N_t \times N_t$ UCA channel and is thus not shown. For reference, capacity curves for the ideal case ($\sigma_k = \sqrt{N_t}$ for all $1 \le k \le N_t$) and for the $N_t \times N_t$ UCA channel with $\Delta\theta = 0$ are provided. We see that the relations among these curves are different for these three β values. Focusing on high SNR, all best-case capacity curves run parallel to the ideal one, with small SNR penalties due to slight singular value dispersion well-matching the ellipticity results shown in Fig. 7 (b) and (e). For instance, with $\beta = 7.2$, the best-case nonUCA channel capacity practically overlaps with the ideal curve and is strictly better than the best-case UCA channels. For the other two β values, one of the best-case UCA channels comes close to the best-case nonUCA channel, but a small gap to the ideal case remains. The more significant differences appear in the worst-case capacity curves. As noted in Remark 3, as N_t is even, the worst-case $N_t \times N_t$ UCA channel has a zero singular value, resulting in a slower capacity increase with SNR. For $\beta = 7.2$, the capacity curve is notably poorer than the others, indicating the loss of more than one DOF. (The squared singular values in descending order for this channel are 34.933, 0.531, 0.531, 0.002, 0.002, and 0.) This scenario illustrates that a larger β does not necessarily enhance performance, highlighting a key characteristic of the UCA channel. We can conclude that, if the angular offsets can be optimized, all schemes perform close to optimal (within 0.5 dB), and the non-UCA scheme will not be significantly better than a UCA scheme. However, if angular offsets are not optimized, this may result in poor ellipticity and, in extreme cases, loss of one or several effective DOFs and thereby significant loss of capacity.

Fig. 10 compares the channel capacity performance of an $N_t \times N_t$ UCA channel, as N_t increases, with that of a CCA channel. The capacities are calculated at $\mathrm{SNR}_0(P_\mathrm{T}/N_t) = 30$ dB, with total transmit power scaling linearly with N_t, for a fixed β and three angular offsets: $\Delta\theta$: $\Delta\theta = 0$, π/N_t, and

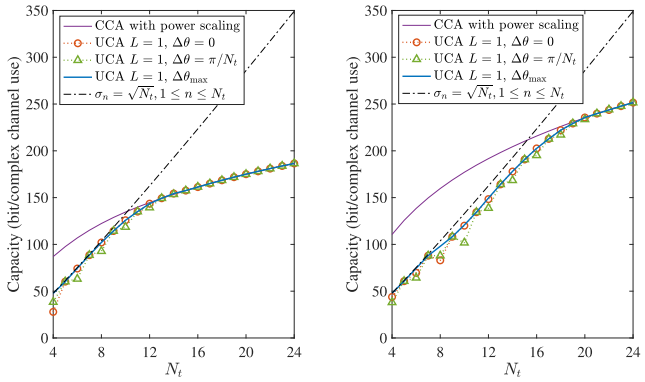

(a) $\beta = 3$ (b) $\beta = 5.5$

Fig. 10. Capacity performance of a $N_t \times N_t$ UCA channel with fixed β and increasing N_t, at $\mathrm{SNR}_0(P_\mathrm{T}/N_t) = 30$ dB.

$\Delta\theta_{\max}$ (determined via grid search). The CCA channel singular values, given by (25), are scaled by $N_t/2\pi$ to match the UCA channel power gain, ensuring $\sum_{n\in\mathbb{Z}} \left(\frac{N_t}{2\pi}\gamma_n(\beta)\right)^2 = N_t^2$. The CCA capacity is found by waterfilling power allocation over all CCA channel DOFs. Hence, for small N_t, the CCA scheme has access to more spatial multiplexing compared to the ideal $N_t \times N_t$ MIMO scheme, which is limited to N_t DOFs. This explains why the CCA capacity is higher than the ideal MIMO capacity for small N_t. However, the ideal MIMO channel capacity increases linearly with N_t and will eventually surpass the CCA capacity. This is because of the severe decrease of the sorted CCA channel singular values $\gamma_{n(N_t)}$ for large N_t, as discussed in Sec. II-B2 and II-B3. Initially, for small N_t, the UCA channel capacity with optimally-adjusted $\Delta\theta_{\max}$ grows at the same rate as the ideal $N_t \times N_t$ MIMO channel. Beyond a certain point, growth slows, and the UCA capacity converges with the CCA capacity, indicating a lack of additional spatial DOF gain from more antennas. The N_t value where this slowdown begins represents the effective DOF of the CCA channel, aligning well with estimates from (21). With fixed $\Delta\theta$, the UCA channel capacity does not necessarily increase with

N_t. The DOF loss caused by $\Delta\theta = \pi/N_r$ for any even N_t leads to noticeable capacity drops. In oversampling scenarios where the number of antennas exceed the available effective DOFs, angular offset no longer affects capacity: Equation (54) shows an effective one-to-one mapping between non-zero CCA and UCA singular values via phase-shifting by the angular offset, which does not alter their magnitudes.

VI. Conclusion

When the communication distance $D \gg \max(R_t, R_r)$, the narrowband CCA channel behaves as a bounded linear normal operator characterized by $\beta = 2\pi R_t R_r/\lambda D$. Spectral analysis shows an infinite number of OAM eigenmodes with eigenvalues determined by first-kind Bessel functions evaluated at β. On this basis, we derived exact analytical expressions for the singular values of LOS MIMO channels with discrete circular antenna arrays in two configurations: one with $N_r = LN_t$ receive antennas arranged in a UCA, and another with antennas forming L sub-UCAs, each with N_t elements. These expressions provide an accurate characterization of the channel behavior by accounting for the dependence of the discrete singular values on β, the number of antennas, and the angular offset of the receiving UCA or sub-UCA via a sum of phase-shifted Bessel functions. DFT precoding and combining are shown to be optimal for achieving capacity in both setups, and specific transceiver structures are provided.

Numerical evaluations revealed several interesting insights in the high-SNR regime:

- **Non-Monotonic CCA DOFs:** The number of available DOFs, i.e., the number of significant singular values in the CCA channel generally increase with β, but not in a monotonic fashion. Hence, the estimated number of DOFs given by (21) should be used with care.
- **Intricate MIMO Capacity Behavior:** Discrete LOS MIMO channel capacity does not necessarily increase with β or with the the number of antennas. Capacity can sometimes be improved by reducing β, e.g., by reducing the array radii. Moreover, even before the number of antennas exceeds the number of available DOFs, increasing the number of antennas does not necessarily lead to higher capacity if power gain effects are excluded.
- **High Sensitivity to Angular Offsets:** Channel capacity is highly sensitive to angular offsets, especially in $N_t \times N_t$ systems, where loss of one or more effective DOFs can occur in the worst case.
- **Limited Sub-UCA Benefits:** After optimizing the angular offsets, the multiple sub-UCA design perform as well as or better than the single UCA design for $N_t \times LN_t$ systems, but the performance improvement is minimal except for certain deployments.

It is worth emphasizing that the communication distance, array radii, number of antennas, antenna arrangement, and angular offsets can either be fixed or adjustable in different scenarios, and it is important to consider these nuances when interpreting numerical results.

This study analyzes a monochromatic, single-polarization LOS link under ideal conditions. Several key extensions remain open: (i) *Wideband operation:* Because β varies with wavelength, both eigenmodes and capacity-achieving transceivers are inherently frequency-dependent. Quantifying performance over realistic wideband channels is crucial for high-data-rate deployments [36]. (ii) *Misalignment tolerance:* In addition to the lateral offset (communication range) and rotational misalignment (angular offset) discussed in this paper, real links also experience tilt and axial offsets. A unified analytical framework that captures these factors and their impact on capacity is lacking. (iii) *High-dimensional offset optimization:* Extending the L-sub-UCA receiver structure to $L > 2$ is straightforward but leads to a high-dimensional search over angular offset; efficient, near-optimal algorithms remain an open challenge. (iv) *Polarization and array variants:* Dual-polarized elements could potentially double the number of available DOFs, and multiple concentric CCAs/UCAs may further enrich the eigenstructure. Both avenues deserve systematic study.

Appendix A
Proof of Theorem 2

To prove Theorem 2, we use the eigendecomposition of the linear operator A in the form of (14), where the expressions of the eigenfunctions $\{\psi_n(\cdot)\}$ and eigenvalues $\{\lambda_n\}$ are given by (15) and (16) in Proposition 1. Substituting (35) into (14), we obtain the electric field over the imaginary CCA as

$$\begin{aligned} y(\theta_r) &= \sum_{n\in\mathbb{Z}} \lambda_n \psi_n(\theta_r) \left\langle \sum_{n_t=0}^{N_t-1} x[n_t]\delta\left(\theta_t - \frac{2\pi}{N_t}n_t\right), \psi_n \right\rangle \\ &= \sum_{n\in\mathbb{Z}} \lambda_n \psi_n(\theta_r) \left(\sum_{n_t=0}^{N_t-1} x[n_t]\psi_n^*\left(\frac{2\pi}{N_t}n_t\right)\right) \\ &= \sum_{n\in\mathbb{Z}} \frac{\sqrt{N_t}}{\sqrt{2\pi}} \lambda_n \psi_n(\theta_r) \left(\boldsymbol{\psi}_{N_t,n}^{\mathrm{H}}\mathbf{x}\right), \end{aligned} \tag{72}$$

where $\mathbf{x} = (x[0], \ldots, x[N_t-1])^{\mathrm{T}}$. Recall that the inner product is defined by (10). Sampling $y(\theta_r)$ at θ_{r,n_r}, we obtain

$$\begin{aligned} y[n_r] &= \sum_{n\in\mathbb{Z}} \frac{\sqrt{N_t}}{\sqrt{2\pi}} \lambda_n \psi_n\left(\frac{2\pi}{N_r}n_r + \Delta\theta\right) \left(\boldsymbol{\psi}_{N_t,n}^{\mathrm{H}}\mathbf{x}\right) \\ &= \sum_{n\in\mathbb{Z}} \frac{\sqrt{N_t}}{2\pi} \lambda_n e^{jn\Delta\theta} e^{jn\frac{2\pi}{N_r}n_r} \left(\boldsymbol{\psi}_{N_t,n}^{\mathrm{H}}\mathbf{x}\right), \end{aligned} \tag{73}$$

which allow us the write $\mathbf{y} = (y[0], \ldots, y[N_r-1])^{\mathrm{T}}$ as

$$\mathbf{y} = \sum_{n\in\mathbb{Z}} \frac{\sqrt{N_t N_r}}{2\pi} \lambda_n e^{jn\Delta\theta} \boldsymbol{\psi}_{N_r,n} \left(\boldsymbol{\psi}_{N_t,n}^{\mathrm{H}}\mathbf{x}\right) \tag{74}$$

Accordingly, we can write the channel matrix as

$$\mathbf{H} = \sum_{n\in\mathbb{Z}} C_n \boldsymbol{\psi}_{N_r,n} \boldsymbol{\psi}_{N_t,n}^{\mathrm{H}}, \tag{75}$$

where

$$C_n = \frac{\sqrt{N_t N_r}}{2\pi} \lambda_n e^{jn\Delta\theta} = \sqrt{N_t N_r} J_n(\beta) e^{jn\left(\frac{\pi}{2}+\Delta\theta\right)}. \tag{76}$$

APPENDIX B
PROOF OF THEOREM 3

From (47), (41), and (18), it follows that

$$Z_{k_t,k_r} = \boldsymbol{\psi}_{N_r,k_r}^{\mathrm{H}} \left(\sum_{n\in\mathbb{Z}} C_n \boldsymbol{\psi}_{N_r,n} \boldsymbol{\psi}_{N_t,n}^{\mathrm{H}} \right) \boldsymbol{\psi}_{N_t,k_t} = \sum_{n\in\mathbb{Z}} C_n (\boldsymbol{\psi}_{N_r,k_r}^{\mathrm{H}} \boldsymbol{\psi}_{N_r,n})(\boldsymbol{\psi}_{N_t,n}^{\mathrm{H}} \boldsymbol{\psi}_{N_t,k_t}) \tag{77}$$

It follows from the remarks under (43) that the nth term in (77) equals to C_n if and only if $k_t - n \in N_t\mathbb{Z}$ and $n - k_r \in N_r\mathbb{Z}$ and is zero otherwise. Phrased differently, if n satisfies the system of equations

$$k_t - n = pN_t \tag{78a}$$

$$n - k_r = qN_r \tag{78b}$$

for some $p, q \in \mathbb{Z}$, then Z_{k_t,k_r} can be nonzero. Conversely, if (78) has no solution, then $Z_{k_t,k_r} = 0$.

From the generalization of the Chinese remainder theorem proven in [37, Theorem 1.7], we know that (78) has a solution if and only if $m = k_t - k_r \in N_{\mathrm{gcd}}\mathbb{Z}$. Moreover, if $n = n_0$ is a particular solution to (78), then the complete solution set is $n_0 + N_{\mathrm{lcm}}\mathbb{Z}$.

Hence, if $m \notin N_{\mathrm{gcd}}\mathbb{Z}$, (78) has no solution, which implies that $Z_{k_t,k_r} = 0$, and the lower case in (48) is proven.

Now suppose $m = rN_{\mathrm{gcd}}$ for an $r \in \mathbb{Z}$, which implies that $m \in N_{\mathrm{gcd}}\mathbb{Z}$. We proceed to find a particular solution $n = n_0$ to (78). Adding (78a) and (78b) yields

$$m = k_t - k_r = pN_t + qN_r. \tag{79}$$

From Bézout's identity [37, Theorem 1.7], we have

$$N_{\mathrm{gcd}} = p_1 N_t + q_1 N_r \tag{80}$$

where p_1, q_1 are found from the extended Euclidean algorithm[10]. Multiplying both sides of (80) with r yields

$$m = rN_{\mathrm{gcd}} = rp_1 N_t + rq_1 N_r, \tag{81}$$

and we identify $(p, q) = (rp_1, r\,q_1)$ as a solution to (79). Hence, a particular solution to (78) is found by substituting $p = rp_1$ into (78a) and solving for n:

$$n = n_0 = k_t - pN_t = k_t - \frac{m}{N_{\mathrm{gcd}}} p_1 N_t. \tag{82}$$

(It is easily checked that $n = n_0$ also satisfies (78b).) Hence, all solutions to (78) lies in the set

$$\mathcal{N}_{k_t,m}^{*} = n_0 + N_{\mathrm{lcm}}\mathbb{Z} = \left(k_t - mp_1 \frac{N_t}{N_{\mathrm{gcd}}} \right) + N_{\mathrm{lcm}}\mathbb{Z} \tag{83}$$

which proves the upper case in (48) and completes the proof of the theorem.

[10]In MATLAB, we can compute N_{gcd}, p_1, and q_1 as `[Ngcd, p1, q1] = gcd(Nt, Nr)`.

APPENDIX C
PROOF OF THE EXISTENCE OF THE ZERO SINGULAR VALUE IN THE SPECIAL CASE STATED IN REMARK 3

We prove that for a UCA channel, if $N_t = N_r$ is an even number and $\Delta\theta = \frac{\pi}{N_r}$, then $\sigma_{N_t/2} = |Z_{N_t/2,N_t/2}| \equiv 0$ for all β. To simplify notation, we let $\eta(N_t, m, \Delta\theta) \triangleq \left(\frac{N_t}{2} + mN_t\right)\left(\frac{\pi}{2} + \Delta\theta\right)$ and drop the arguments when there is no risk of confusion. Based on (54), we can rewrite $Z_{N_t/2,N_t/2}$ as

$$Z_{N_t/2,N_t/2} = N_t \sum_{m\in\mathbb{N}} \left[e^{j\eta} J_{N_t/2+mN_t}(\beta) + e^{-j\eta} J_{-(N_t/2+mN_t)}(\beta) \right]. \tag{84}$$

Since $J_{-n}(\beta) = (-1)^n J_n(\beta)$ for nonzero n and mN_t is even,

$$\begin{aligned} Z_{N_t/2,N_t/2} &= N_t \sum_{m\in\mathbb{N}} \left[e^{j\eta} J_{N_t/2+mN_t}(\beta) + (-1)^{\frac{N_t}{2}} e^{-j\eta} J_{N_t/2+mN_t}(\beta) \right] \\ &= \begin{cases} 2\,N_t \cos\eta \sum_{m\in\mathbb{N}} J_{N_t/2+mN_t}(\beta), & \frac{N_t}{2} \text{is even}, \\ 2jN_t \sin\eta \sum_{m\in\mathbb{N}} J_{N_t/2+mN_t}(\beta), & \frac{N_t}{2} \text{is odd}. \end{cases} \end{aligned} \tag{85}$$

Substituting $\Delta\theta = \frac{\pi}{N_r} = \frac{\pi}{N_t}$ into $\eta(N_t, m, \Delta\theta)$, we have

$$\eta(N_t, m, \Delta\theta) = \left(\frac{N_t}{2} + 1\right)\frac{\pi}{2} + \left(\frac{mN_t}{2} + m\right)\pi \tag{86}$$

where $\left(\frac{mN_t}{2} + m\right)$ is an integer since N_t is even. Therefore, if $N_t/2$ is even, $\cos\eta = 0$, and if $N_t/2$ is odd, $\sin\eta = 0$. As a result, $Z_{N_t/2,N_t/2} = 0$ for all β.

ACKNOWLEDGMENT

The authors want to acknowledge the valuable comments from the editor and the anonymous reviewers, which allowed them to improve the quality of the article. In particular, the proof of Theorem 3 was made more elegant and compact compared to the original submission.

REFERENCES

[1] L. Ding, A. R. Vilenskiy, R. Devassy, M. Coldrey, T. Eriksson, and E. G. Ström, "Shannon capacity of LOS MIMO channels with uniform circular arrays," in *Proc. IEEE 33rd Annu. Int. Symp. Pers., Indoor Mobile Radio Commun. (PIMRC)*, Sep. 2022, pp. 1–7.

[2] L. Ding, E. G. Ström, and J. Zhang, "Degrees of freedom in 3D linear large-scale antenna array communications—A spatial bandwidth approach," *IEEE J. Sel. Areas Commun.*, vol. 40, no. 10, pp. 2805–2822, Oct. 2022.

[3] L. Ding, J. Zhang, and E. G. Ström, "Spatial bandwidth asymptotic analysis for 3D large-scale antenna array communications," *IEEE Trans. Wireless Commun.*, vol. 23, no. 4, pp. 2638–2652, Apr. 2024.

[4] F. Bohagen, P. Orten, and G. E. Oien, "Construction and capacity analysis of high-rank line-of-sight MIMO channels," in *Proc. IEEE Wireless Commun. Netw. Conf.*, vol. 1, Mar. 2005, pp. 432–437.

[5] F. Bohagen, P. Orten, and G. E. Oien, "Design of optimal high-rank line-of-sight MIMO channels," *IEEE Trans. Wireless Commun.*, vol. 6, no. 4, pp. 1420–1425, Apr. 2007.

[6] H. Do, S. Cho, J. Park, H.-J. Song, N. Lee, and A. Lozano, "Terahertz line-of-sight MIMO communication: Theory and practical challenges," *IEEE Commun. Mag.*, vol. 59, no. 3, pp. 104–109, Mar. 2021.

[7] P. Wang, Y. Li, and B. Vucetic, "Millimeter wave communications with symmetric uniform circular antenna arrays," *IEEE Commun. Lett.*, vol. 18, no. 8, pp. 1307–1310, Aug. 2014.

[8] R. Chen, W.-X. Long, X. Wang, and L. Jiandong, "Multi-mode OAM radio waves: Generation, angle of arrival estimation and reception with UCAs," *IEEE Trans. Wireless Commun.*, vol. 19, no. 10, pp. 6932–6947, Oct. 2020.
[9] Y. Jeon, G.-T. Gil, and Y. H. Lee, "Design and analysis of LoS-MIMO systems with uniform circular arrays," *IEEE Trans. Wireless Commun.*, vol. 20, no. 7, pp. 4527–4540, Jul. 2021.
[10] H. Sasaki, Y. Yagi, H. Fukumoto, and D. Lee, "OAM-MIMO multiplexing transmission system for high-capacity wireless communications on millimeter-wave band," *IEEE Trans. Wireless Commun.*, vol. 23, no. 5, pp. 3990–4003, May 2024.
[11] B. Thidé et al., "Utilization of photon orbital angular momentum in the low-frequency radio domain," *Phys. Rev. Lett.*, vol. 99, no. 8, Aug. 2007, Art. no. 087701.
[12] S. M. Mohammadi et al., "Orbital angular momentum in radio—A system study," *IEEE Trans. Antennas Propag.*, vol. 58, no. 2, pp. 565–572, Feb. 2010.
[13] O. Edfors and A. J. Johansson, "Is orbital angular momentum (OAM) based radio communication an unexploited area?," *IEEE Trans. Antennas Propag.*, vol. 60, no. 2, pp. 1126–1131, Feb. 2012.
[14] D. Lee, H. Sasaki, H. Fukumoto, Y. Yagi, and T. Shimizu, "An evaluation of orbital angular momentum multiplexing technology," *Appl. Sci.*, vol. 9, no. 9, p. 1729, Apr. 2019.
[15] Y. Yagi, H. Sasaki, T. Yamada, and D. Lee, "200 Gb/s wireless transmission using dual-polarized OAM-MIMO multiplexing with uniform circular array on 28 GHz band," *IEEE Antennas Wireless Propag. Lett.*, vol. 20, pp. 833–837, 2021.
[16] M. Hirabe, R. Zenkyu, H. Miyamoto, K. Ikuta, and E. Sasaki, "40 m transmission of OAM mode and polarization multiplexing in E-band," in *Proc. IEEE Globecom Workshops (GC Wkshps)*, Dec. 2019, pp. 1–6.
[17] M. Palaiologos, M. H. Castañeda García, A. Kakkavas, R. A. Stirling-Gallacher, and G. Caire, "Robust non-uniform LoS MIMO array design," *IEEE Trans. Wireless Commun.*, vol. 23, no. 10, pp. 13202–13218, Oct. 2024.
[18] L. Zhou and Y. Ohashi, "Low complexity millimeter-wave LOS-MIMO precoding systems for uniform circular arrays," in *Proc. IEEE Wireless Commun. Netw. Conf. (WCNC)*, Apr. 2014, pp. 1293–1297.
[19] L. Zhou and Y. Ohashi, "Performance analysis of mmWave LOS-MIMO systems with uniform circular arrays," in *Proc. IEEE 81st Veh. Technol. Conf. (VTC Spring)*, May 2015, pp. 1–5.
[20] R. Chen, H. Xu, M. Moretti, and J. Li, "Beam steering for the misalignment in UCA-based OAM communication systems," *IEEE Wireless Commun. Lett.*, vol. 7, no. 4, pp. 582–585, Aug. 2018.
[21] H. Jing, W. Cheng, and X.-G. Xia, "A simple channel independent beamforming scheme with parallel uniform circular array," *IEEE Commun. Lett.*, vol. 23, no. 3, pp. 414–417, Mar. 2019.
[22] L. Zhu and J. Zhu, "Optimal design of uniform circular antenna array in mmWave LOS MIMO channel," *IEEE Access*, vol. 6, pp. 61022–61029, 2018.
[23] M. Palaiologos, M. H. C. Garcia, R. A. Stirling-Gallacher, and G. Caire, "Design of robust LoS MIMO systems with UCAs," in *Proc. IEEE 94th Veh. Technol. Conf. (VTC-Fall)*, Sep. 2021, pp. 1–5.
[24] A. S. Y. Poon, R. W. Brodersen, and D. N. C. Tse, "Degrees of freedom in multiple-antenna channels: A signal space approach," *IEEE Trans. Inf. Theory*, vol. 51, no. 2, pp. 523–536, Feb. 2005.
[25] D. A. B. Miller, "Waves, modes, communications, and optics: A tutorial," *Adv. Opt. Photon.*, vol. 11, no. 3, pp. 679–825, Sep. 2019.
[26] S. J. Bernau, "The spectral theorem for normal operators," *J. London Math. Soc.*, vol. 1, no. 1, pp. 478–486, 1965.
[27] R. Whitley, "The spectral theorem for a normal operator," *Amer. Math. Monthly*, vol. 75, no. 8, pp. 856–861, Oct. 1968.
[28] A. Lapidoth, *A Foundation in Digital Communication*. Cambridge, U.K.: Cambridge Univ. Press, 2017.
[29] M. Abramowitz and I. A. Stegun, *Handbook of Mathematical Functions With Formulas, Graphs, and Mathematical Tables*. U.S. Government Printing Office, 1972.
[30] L. W. Couch, *Digital and Analog Communication Systems*. Upper Saddle River, NJ, USA: Prentice-Hall, 1997.
[31] H. Do, N. Lee, and A. Lozano, "Line-of-sight MIMO via intelligent reflecting surface," *IEEE Trans. Wireless Commun.*, vol. 22, no. 6, pp. 4215–4231, Jun. 2023.
[32] D. Tse and P. Viswanath, *Fundamentals Wireless Communication*. Cambridge, U.K.: Cambridge Univ. Press, 2005.
[33] H. Lütkepohl, *Handbook Matrices*. Hoboken, NJ, USA: Wiley, 1996.
[34] J. Salo, P. Suvikunnas, H. El-Sallabi, and P. Vainikainen, "Some insights into MIMO mutual information: The high SNR case," *IEEE Trans. Wireless Commun.*, vol. 5, no. 10, pp. 2997–3001, Nov. 2006.
[35] S. Rao, D. Wilton, and A. Glisson, "Electromagnetic scattering by surfaces of arbitrary shape," *IEEE Trans. Antennas Propag.*, vol. AP-30, no. 3, pp. 409–418, May 1982.
[36] T. Ingason, H. Liu, M. Coldrey, A. Wolfgang, and J. Hansryd, "Impact of frequency selective channels on a line-of-sight MIMO microwave radio link," in *Proc. IEEE 71st Veh. Technol. Conf.*, May 2010, pp. 1–5.
[37] G. A. Jones and J. M. Jones, *Elementary Number Theory*. London, U.K.: Springer, 1998.

Liqin Ding received the Ph.D. degree in information and communication engineering from Harbin Institute of Technology, Harbin, China, in 2017. From 2017 to 2019, she was a Post-Doctoral Researcher at the School of Electronic and Information Engineering, Harbin Institute of Technology, Shenzhen, China. From 2019 to 2024, she was a Marie Skłodowska-Curie Fellow (MSCA-IF) and a Researcher with the Communication Systems Group, Department of Electrical Engineering, Chalmers University of Technology, Gothenburg, Sweden. She is currently a Senior Researcher with Ericsson Research, Ericsson AB, Lund, Sweden. Her research interests cover various areas in signal processing and wireless communication, with a particular focus on antenna array-based communication technologies.

Rahul Devassy received the B.Tech. degree in electrical and electronics engineering from the National Institute of Technology Calicut, India, in 2006, the M.E. degree in telecommunication from Indian Institute of Science at Bengaluru, Bengaluru, India, in 2009, and the Ph.D. degree in electrical engineering from the Chalmers University of Technology, Gothenburg, Sweden, in 2019. He joined Ericsson AB in 2019, where he is currently a Senior Researcher involved in wireless transport network research and 6G standardization efforts. His research interests include information and communication theory.

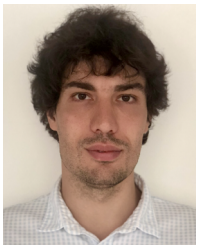

Artem R. Vilenskiy (Senior Member, IEEE) received the Specialist degree (summa cum laude) in radio engineering and the Ph.D. degree in antennas and microwave devices from Bauman Moscow State Technical University, Moscow, Russia, in 2011 and 2014, respectively.

From 2011 to 2019, he was with Samsung Research Institute Russia, Moscow, where he had roles of a Researcher, a Expert Engineer, and a Project Leader at the Electromagnetics Group and RF Sensor Part. From 2015 to 2019, he was a visiting Associate Professor at the Radio-Electronic Systems and Devices Department, Bauman Moscow State Technical University. From 2019 to 2024, he was a Researcher with Antenna Systems Group, Chalmers University of Technology, Gothenburg, Sweden. He is currently a Microwave Team Lead at XPANCEO, Dubai, United Arab Emirates. His research interests include applied and computational electromagnetics, antenna and front-end integrated circuit design, and controllable high-frequency materials and devices.

Mikael Coldrey received the M.Sc. degree in applied physics and electrical engineering from Linköping University, Linköping, Sweden, in 2000, and the Ph.D. degree in electrical engineering from the Chalmers University of Technology, Gothenburg, Sweden, in 2006. He joined Ericsson Research in 2006, where he is currently a Principal Researcher. From 2017 to 2020, he was the Head of the Microwave Systems Research Section, Ericsson Research. He received the Docent (habilitation) promotion from Chalmers University of Technology in 2020 and was appointed an Adjunct Professor of communication systems at Chalmers University of Technology. His main research interests are in the areas of wireless communications, signal processing, advanced antenna systems, and millimeter wave communications for radio access and wireless transport systems.

Thomas Eriksson (Member, IEEE) received the Ph.D. degree in information theory from the Chalmers University of Technology, Gothenburg, Sweden, in 1996. From 1990 to 1996, he was at the Chalmers University of Technology. From 1997 to 1998, he was at AT&T Labs-Research, Murray Hill, NJ, USA. From 1998 to 1999, he was at Ericsson Radio Systems AB, Kista, Sweden. Since 1999, he has been with Chalmers University of Technology, where he is currently a Professor of communication systems. He was a Guest Professor with Yonsei University, South Korea, from 2003 to 2004. He has authored or co-authored more than 300 journal and conference papers and holds 16 patents. He is leading the research on hardware-constrained communications and radar processing with the Chalmers University of Technology. His research interests include communication, radar signal processing, and modeling and compensation of non-ideal hardware components (e.g., amplifiers, oscillators, ADC/DAC, and modulators).

Erik G. Ström (Fellow, IEEE) received the M.S. degree in electrical engineering from the Royal Institute of Technology (KTH), Stockholm, Sweden, in 1990, and the Ph.D. degree in electrical engineering from the University of Florida, Gainesville, in 1994. He accepted a post-doctoral position at the Department of Signals, Sensors, and Systems, KTH, in 1995. In February 1996, he was appointed as an Assistant Professor at KTH, and in June 1996, he joined the Chalmers University of Technology, Gothenburg, Sweden, where he has been a Professor of communication systems since June 2003. He currently heads the Division of Communications, Antennas, and Optical Networks and is the Director of Chalmers' Area-of-Advance Information and Communication Technology. Since 1990, he has acted as a consultant for the Educational Group for Individual Development, Stockholm. His research interests include signal processing and communication theory in general, and constellation labelings, channel estimation, synchronization, multiple access, medium access, multiuser detection, wireless positioning, and vehicular communications in particular. He was a member of the Board of the IEEE VT/COM Swedish Chapter 2000–2006. He received the Chalmers Pedagogical Prize in 1998, the Chalmers Ph.D. Supervisor of the Year Award in 2009, and the Chalmers Area of Advance Award in 2020. He has been a Senior Editor of IEEE TRANSACTION ON INTELLIGENT TRANSPORT SYSTEMS, a contributing author and associate editor for Roy. Admiralty Publishers FesGas-series, and was a Co-Guest Editor for PROCEEDINGS OF THE IEEE special issue on Vehicular Communications in 2011 and IEEE JOURNAL ON SELECTED AREAS IN COMMUNICATIONS special issues on Signal Synchronization in Digital Transmission Systems in 2001 and on Multiuser Detection for Advanced Communication Systems and Networks in 2008.